



FRB 20250316A: A Brilliant and Nearby One-off Fast Radio Burst Localized to 13 pc Precision

Downloaded from: <https://research.chalmers.se>, 2025-09-25 16:01 UTC

Citation for the original published paper (version of record):

Abbott, T., Amouyal, D., Andersen, B. et al (2025). FRB 20250316A: A Brilliant and Nearby One-off Fast Radio Burst Localized to 13 pc Precision. *Astrophysical Journal Letters*, 989(2).
<http://dx.doi.org/10.3847/2041-8213/adf62f>

N.B. When citing this work, cite the original published paper.



FRB 20250316A: A Brilliant and Nearby One-off Fast Radio Burst Localized to 13 pc Precision

The CHIME/FRB Collaboration:

Thomas C. Abbott^{1,2} , Daniel Amouyal^{1,2} , Bridget C. Andersen^{1,2} , Shion E. Andrew^{3,4} , Kevin Bandura^{5,6} , Mohit Bhardwaj⁷ , Kalyani Bhopi^{5,6} , Yash Bhusare⁸ , Charanjot Brar⁹ , Alice Cai^{10,11} , Tomas Cassanelli¹² , Shami Chatterjee¹³ , Jean-François Cliche^{1,2} , Amanda M. Cook^{1,2,14} , Alice P. Curtin^{1,2} , Evan Davies-Veile^{1,2} , Matt Dobbs^{1,2} , Fengqiu Adam Dong¹⁵ , Yuxin Dong (董雨欣)^{10,11} , Gwendolyn Eadie^{16,17,18} , Tarraneh Eftekhari¹¹ , Wen-fai Fong^{10,11} , Emmanuel Fonseca^{6,19} , B. M. Gaensler^{16,20,21} , Nina Gusinskaia^{14,22} , Jason W. T. Hessels^{1,2,14,22} , Danté M. Hewitt¹⁴ , Jeff Huang^{1,2} , Naman Jain^{1,2} , Ronniy. C. Joseph^{1,2} , Lordrick Kahinga²⁰ , Victoria M. Kaspi^{1,2} , Afrasiyab (Afrokk) Khan^{1,2} , Bikash Kharel^{6,19} , Adam E. Lanman^{3,4} , Magnus L'Argent^{1,2} , Mattias Lazda^{16,21} , Calvin Leung^{23,24} , Robert Main^{1,2} , Lluís Mas-Ribas²⁰ , Kiyoshi W. Masui^{3,4} , Kyle McGregor^{1,2} , Ryan Mckinven^{1,2} , Juan Mena-Parra^{16,21} , Daniele Michilli²⁵ , Nicole Mulyk^{1,2} , Mason Ng^{1,2,29} , Kenzie Nimmo³ , Ayush Pandhi^{16,21} , Swarali Shivraj Patil^{6,19} , Aaron B. Pearlman^{1,2} , Ue-Li Pen^{21,26,27,28,29} , Ziggy Pleunis^{14,22} , J. Xavier Prochaska^{20,30,31} , Masoud Rafiei-Ravandi¹ , Scott M. Ransom¹⁵ , Gurman Sachdeva^{16,21} , Mawson W. Sammons^{1,2} , Ketan R. Sand^{1,2} , Paul Scholz^{21,32} , Vishwangi Shah^{1,2} , Kaitlyn Shin^{3,4} , Seth R. Siegel^{1,2,29} , Sunil Simha^{11,33} , Kendrick Smith²⁹ , Ingrid Stairs³⁴ , David C. Stenning³⁵ , Haochen Wang^{3,4} , Thomas Boles³⁶ , Ismaël Cognard^{37,38} , Tammo Jan Dijkema²² , Alexei V. Filippenko²⁴ , Marcin P. Gawroński³⁹ , Wolfgang Herrmann⁴⁰ , Charles D. Kilpatrick¹¹ , Franz Kirsten^{22,41} , Shawn Knabel⁴² , Omar S. Ould-Boukattine^{14,22} , Hadrien Pagnat⁴² , Weronika Puchalska³⁹ , William Sheu⁴² , Aswin Suresh^{10,11} , Aaron Tohuavohu⁴³ , Tommaso Treu⁴² , and WeiKang Zheng²⁴

¹ Department of Physics, McGill University, 3600 rue University, Montréal, QC H3A 2T8, Canada; amanda.cook@mail.mcgill.ca

² Trottier Space Institute, McGill University, 3550 rue University, Montréal, QC H3A 2A7, Canada

³ MIT Kavli Institute for Astrophysics and Space Research, Massachusetts Institute of Technology, 77 Massachusetts Avenue, Cambridge, MA 02139, USA

⁴ Department of Physics, Massachusetts Institute of Technology, 77 Massachusetts Avenue, Cambridge, MA 02139, USA

⁵ Lane Department of Computer Science and Electrical Engineering, 1220 Evansdale Drive, PO Box 6109, Morgantown, WV 26506, USA

⁶ Center for Gravitational Waves and Cosmology, West Virginia University, Chestnut Ridge Research Building, Morgantown, WV 26505, USA

⁷ McWilliams Center for Cosmology & Astrophysics, Department of Physics, Carnegie Mellon University, Pittsburgh, PA 15213, USA

⁸ National Centre for Radio Astrophysics, Post Bag 3, Ganeshkhind, Pune, 411007, India

⁹ National Research Council of Canada, Herzberg Astronomy and Astrophysics, 5071 West Saanich Road, Victoria, BC V9E 2E7, Canada

¹⁰ Department of Physics and Astronomy, Northwestern University, Evanston, IL 60208, USA

¹¹ Center for Interdisciplinary Exploration and Research in Astronomy, Northwestern University, 1800 Sherman Avenue, Evanston, IL 60201, USA

¹² Department of Electrical Engineering, Universidad de Chile, Av. Tupper 2007, Santiago 8370451, Chile

¹³ Cornell Center for Astrophysics and Planetary Science, Cornell University, Ithaca, NY 14853, USA

¹⁴ Anton Pannekoek Institute for Astronomy, University of Amsterdam, Science Park 904, 1098 XH Amsterdam, The Netherlands

¹⁵ National Radio Astronomy Observatory, 520 Edgemont Road, Charlottesville, VA 22903, USA

¹⁶ David A. Dunlap Department of Astronomy and Astrophysics, 50 St. George Street, University of Toronto, ON M5S 3H4, Canada

¹⁷ Department of Statistical Sciences, University of Toronto, Toronto, ON M5S 3G3, Canada

¹⁸ Data Sciences Institute, University of Toronto, 17th Floor, Ontario Power Building, 700 University Avenue, Toronto, ON M5G 1Z5, Canada

¹⁹ Department of Physics and Astronomy, West Virginia University, PO Box 6315, Morgantown, WV 26506, USA

²⁰ Department of Astronomy and Astrophysics, University of California, Santa Cruz, 1156 High Street, Santa Cruz, CA 95060, USA

²¹ Dunlap Institute for Astronomy and Astrophysics, 50 St. George Street, University of Toronto, ON M5S 3H4, Canada

²² ASTRON, Netherlands Institute for Radio Astronomy, Oude Hoogeveensedijk 4, 7991 PD Dwingeloo, The Netherlands

²³ Miller Institute for Basic Research in Science, Stanley Hall, Room 206B, Berkeley, CA 94720, USA

²⁴ Department of Astronomy, University of California, Berkeley, CA 94720-3411, USA

²⁵ Laboratoire d'Astrophysique de Marseille, Aix-Marseille Univ., CNRS, CNES, Marseille, France

²⁶ Institute of Astronomy and Astrophysics, Academia Sinica, Astronomy-Mathematics Building, No. 1, Sec. 4, Roosevelt Road, Taipei 10617, Taiwan

²⁷ Canadian Institute for Theoretical Astrophysics, 60 St. George Street, Toronto, ON M5S 3H8, Canada

²⁸ Canadian Institute for Advanced Research, 180 Dundas Street West, Toronto, ON M5G 1Z8, Canada

²⁹ Perimeter Institute of Theoretical Physics, 31 Caroline Street North, Waterloo, ON N2L 2Y5, Canada

³⁰ Kavli Institute for the Physics and Mathematics of the Universe (Kavli IPMU), 5-1-5 Kashiwanoha, Kashiwa, 277-8583, Japan

³¹ Division of Science, National Astronomical Observatory of Japan, 2-21-1 Osawa, Mitaka, Tokyo 181-8588, Japan

³² Department of Physics and Astronomy, York University, 4700 Keele Street, Toronto, ON M3J 1P3, Canada

³³ Department of Astronomy and Astrophysics, University of Chicago, William Eckhardt Research Center, 5640 South Ellis Avenue, Chicago, IL 60637, USA

³⁴ Department of Physics and Astronomy, University of British Columbia, 6224 Agricultural Road, Vancouver, BC V6T 1Z1, Canada

³⁵ Department of Statistics and Actuarial Science, Simon Fraser University, 8888 University Drive West, Burnaby, BC V5A 1S6, Canada

³⁶ Coddanham Observatories, Peel House, High Street Coddanham, Suffolk, IP6 9QY, UK

³⁷ LPC2E, OSUC, Univ Orleans, CNRS, CNES, Observatoire de Paris, F-45071 Orleans, France

³⁸ Observatoire Radioastronomique de Nançay, Observatoire de Paris, Université PSL, Université d'Orléans, CNRS, 18330 Nançay, France

³⁹ Institute of Astronomy, Faculty of Physics, Astronomy and Informatics, Nicolaus Copernicus University, Grudziadzka 5, PL-87-100 Toruń, Poland

⁴⁰ Astropheiler Stockert e.V. Astropheiler 1-4, 53903 Bad Münstereifel, Germany

⁴¹ Department of Space, Earth and Environment, Chalmers University of Technology, Onsala Space Observatory, 439 92, Onsala, Sweden

⁴² Department of Physics and Astronomy, University of California, Los Angeles, CA 90095, USA⁴³ Cahill Center for Astronomy and Astrophysics, California Institute of Technology, Pasadena, CA 91125, USA

Received 2025 June 23; revised 2025 July 24; accepted 2025 July 31; published 2025 August 21

Abstract

Precise localizations of a small number of repeating fast radio bursts (FRBs) using very long baseline interferometry (VLBI) have enabled multiwavelength follow-up observations revealing diverse local environments. However, the 2%–3% of FRB sources that are observed to repeat may not be representative of the full population. Here we use the VLBI capabilities of the full CHIME Outrigger array for the first time to localize a nearby (40 Mpc), bright (kJy), and apparently one-off FRB source, FRB 20250316A, to its environment on 13 pc scales. We use optical and radio observations to place deep constraints on associated transient emission and the properties of its local environment. We place a 5σ upper limit of $L_{9.9\text{ GHz}} < 2.1 \times 10^{25} \text{ erg s}^{-1} \text{ Hz}^{-1}$ on spatially coincident radio emission, a factor of 100 lower than any known compact persistent radio source associated with an FRB. Our Keck Cosmic Webb Imager observations allow us to characterize the gas density, metallicity, nature of gas ionization, dust extinction, and star formation rate through emission line fluxes. We leverage the exceptional brightness and proximity of this source to place deep constraints on the repetition of FRB 20250316A and find that it is inconsistent with all well-studied repeaters given the nondetection of bursts at lower spectral energies. We explore the implications of a measured offset of 190 ± 20 pc from the center of the nearest star formation region in the context of progenitor channels. FRB 20250316A marks the beginning of an era of routine localizations for one-off FRBs on tens of milliarcseconds scales, enabling large-scale studies of their local environments.

Unified Astronomy Thesaurus concepts: [Radio bursts \(1339\)](#); [Transient detection \(1957\)](#); [Supernova remnants \(1667\)](#); [Interstellar medium \(847\)](#); [Compact objects \(288\)](#); [Star forming regions \(1565\)](#)

1. Introduction

Fast radio bursts (FRBs) are roughly millisecond-duration flashes of radio waves with Jy-level peak fluxes originating from cosmological distances (D. R. Lorimer et al. 2007). The implied typical isotropic emitting energies of 10^{36} – 10^{42} erg (e.g., D. Thornton et al. 2013; S. D. Ryder et al. 2023; K. Shin et al. 2023) prompted many early interpretations to favor cataclysmic origins. However, the discovery of the first repeating FRB challenged this picture, immediately ruling out cataclysmic theories for that source (L. G. Spitler et al. 2016). Since then, we have discovered roughly 4000 unique FRBs, of which we have identified ~ 100 as repeaters (CHIME/FRB Collaboration et al. 2021, 2023, 2025b; A. M. Cook et al. 2025, in preparation). Even still, the answers to fundamental questions, such as “Do all FRBs arise from a single progenitor class?”, “Do all FRBs repeat?”, and “What are the sources of FRBs?”, remain elusive.

There is a clear phenomenological difference in apparent one-off FRBs and repeaters: bursts from repeaters are statistically narrower in bandwidth and longer in duration than apparent one-offs⁴⁴ (Z. Pleunis et al. 2021; A. P. Curtin et al. 2024). Compared to one-off FRBs, some of the most active repeaters appear anomalous given their association with compact persistent radio sources (PRSs; B. Marcote et al. 2017; C. H. Niu et al. 2022; S. Bhandari et al. 2023; G. Bruni et al. 2024, 2025b) and extreme magnetoionic environments, as evidenced by high and variable Faraday rotation measure (RM) values (D. Michilli et al. 2018;

R. Anna-Thomas et al. 2023). There also are hints of differences in host galaxy populations (repeater hosts may have generally lower stellar masses and optical luminosities; A. C. Gordon et al. 2023; M. Bhardwaj et al. 2024b; D. M. Hewitt et al. 2024a; K. Sharma et al. 2024), but the significance is currently marginal.

On the other hand, high-cadence, long-exposure studies of repeaters have shown flattening power-law slopes in burst energy distributions toward higher energies (above $E_\nu \approx 10^{32} \text{ erg Hz}^{-1}$), which relieves tension between the two phenomena, suggesting that one-off FRB sources may simply be the rarest/highest-energy bursts from repeaters (F. Kirsten et al. 2024; O. S. Ould-Boukattine et al. 2024). Detailed population modeling has shown that assuming all FRBs repeat with some reasonable distribution of rates, one can reproduce the fraction of repeaters to one-offs as well as their dispersion measures (DMs) and declinations (D. W. Gardenier et al. 2021; C. W. James 2023; K. McGregor & D. R. Lorimer 2024; S. Yamasaki et al. 2024).

Environmental studies offer a complementary approach to determine whether one-off FRBs and repeaters originate from distinct progenitor populations. For example, high-resolution studies of the repeating FRBs 20121102A and 20201124A find that they are embedded in regions of active star formation (C. G. Bassa et al. 2017; L. Piro et al. 2021; Y. Dong et al. 2024), in line with models that attribute the emission to a young source, such as a magnetar. This is commensurate with studies of their host galaxy demographics, which find FRBs to primarily arise in star-forming galaxies and trace star formation or a combination of stellar mass and star formation (S. Bhandari et al. 2022; A. C. Gordon et al. 2023; A. Horowitz & B. Margalit 2025; N. Loudas et al. 2025). Moreover, a substantial fraction favor locations in or near spiral arms (A. G. Mannings et al. 2021; M. Bhardwaj et al. 2024b; A. C. Gordon et al. 2025). However, the growing number of FRBs localized to environments without active star formation suggests that some may be formed through delayed channels.

⁴⁴ From this point onward, we refer to these as simply “one-off FRBs” or “nonrepeaters” for conciseness, with the understanding that such a claim is inherently observationally limited and hence “apparent” ought to be implied.



Original content from this work may be used under the terms of the [Creative Commons Attribution 4.0 licence](#). Any further distribution of this work must maintain attribution to the author(s) and the title of the work, journal citation and DOI.

FRB 20180916B, the repeater that exhibits periodic active phases, is located slightly offset (250 ± 190 pc) from the nearest knot of star formation (S. P. Tendulkar et al. 2021). Repeating FRB 20240209A was localized to the outskirts of a quiescent galaxy with a mass-weighted stellar population age of ~ 11 Gyr (T. Eftekhari et al. 2025; V. Shah et al. 2025). FRB 20200120E, the nearest known extragalactic FRB ($d_L = 3.6$ Mpc), was localized to a ~ 9.2 Gyr old globular cluster in the halo of M81 (M. Bhardwaj et al. 2021; F. Kirsten et al. 2022).

Notably, FRB 20200120E and FRB 20240114A, the latter being located in a satellite galaxy of a larger galactic system (M. Bhardwaj et al. 2025), demonstrate that the properties of the local environment of an FRB do not necessarily correlate with the properties of the most massive nearby galaxy.

While these local environment studies have revealed great diversity, such access to tens-of-parsecs-scale localization precision has hitherto been limited to repeaters with high enough burst rates to permit detection in follow-up campaigns with very long baseline interferometry (VBLI) arrays (e.g., B. Marcote et al. 2020; K. Nimmo et al. 2022; D. M. Hewitt et al. 2024b). Only 2%–3% of FRBs have been observed to repeat; even fewer are active enough to have been detected by telescopes other than their discovery machine, and those sources may not be representative of the full population (CHIME/FRB Collaboration et al. 2023).

Recently, construction was completed on three “Outrigger” stations for the Canadian Hydrogen Intensity Mapping Experiment (CHIME) FRB: CHIME-like reflectors oriented to observe the same sky as the core telescope but located on baselines of 66, 956, and 3370 km (A. E. Lanman et al. 2024; CHIME/FRB Collaboration et al. 2025a). The full Outrigger array enables subarcsecond-precision localization for hundreds of FRBs a year and thus host galaxy associations and, for the nearest sources, deep studies of their local environments.

On 2025 March 16, shortly after the final Outrigger station began operating, CHIME/FRB detected its highest-ever signal-to-noise ratio (S/N) extragalactic FRB, FRB 20250316A.⁴⁵ The burst was exceptional only in its source’s proximity, representing an average FRB luminosity. Since the source is nearby and we captured burst data from all four telescope sites, it represents one of the best opportunities to study the local environment of a one-off FRB. The full array provided a 68 mas level localization, corresponding to a projected resolution of 13 pc, the finest physical scale achieved to date for an apparently one-off source.

In this Letter, we describe the radio properties of FRB 20250316A and examine the consistency of the host environment and energetics of this FRB with those of other FRBs, especially the known population of repeating FRBs, leveraging the spatial resolution. In Section 2, we detail the discovery of FRB 20250316A by CHIME/FRB and its 68×57 mas localization. We then detail our deep, multiwavelength follow-up campaign in Section 3. We describe the properties of the radio burst in Section 4, including morphology, polarimetry, and observed two-screen scattering and scintillation. We also constrain the repetition of

the source and compute the V/V_{max} of the burst. In Section 5, we infer the properties of the FRB’s host galaxy (NGC 4141) and local environment. In Section 6, we discuss the multi-wavelength implications of FRB 20250316A and contrast the properties of the local environment to those of the host galaxy more broadly.

2. Discovery of FRB 20250316A

2.1. CHIME/FRB

CHIME is a transit radio telescope operating over 400–800 MHz that surveys the northern sky (i.e., above declinations of -11°) daily (CHIME Collaboration et al. 2022). The FRB backend of CHIME/FRB has enabled the capture of \sim two to three FRBs daily, increasing the total number of known FRB sources from a few dozen to 3649 since its first light in 2018 (CHIME/FRB Collaboration et al. 2025b). The real-time FRB search is described in detail by CHIME/FRB Collaboration et al. (2018).

Upon detection of FRB 20250316A, CHIME/FRB sent triggers to its full Outrigger array, and a VOEvent (T. C. Abbott et al. 2025) was automatically published. FRB 20250316A was extremely bright, which led to its detection above the real-time pipeline $S/N > 8$ in a total of 44 of CHIME/FRB’s 1024 formed beams. The brightness of this burst caused our real-time pipeline to apply a mask over the signal in the two highest-S/N detection beams—an intentional radio frequency interference (RFI) mitigation technique. The masks, however, caused a nonlinear reduction in S/N, and we primarily detected the signal from its “spectral ghosts”: the dispersed spectral leakage originating from the frequency channelization process. This means that the detection S/Ns in these beams are not representative of the true S/N, and the nonlinearity caused the second-brightest beam to be reported as the highest S/N. Using the raw voltage data we captured for the burst at its native $2.56 \mu\text{s}$ resolution, having beamformed the data toward the position of FRB 20250316A (Section 1), dedispersed the data to the FRB’s structure optimizing DM (Section 4), and summed over all frequencies, the peak S/N is 865.

CHIME/FRB had 269.77 hr of exposure toward the position of FRB 20250316A between 2018 August 28 and 2025 May 30 above a fluence sensitivity threshold of 0.5 Jy ms. Details of how we estimate the exposure and sensitivity toward FRB 20250316A are provided in Appendix A.

2.2. CHIME Outriggers and Full-array VLBI Localization

FRB 20250316A marks the first FRB localization achieved using the full CHIME Outrigger array (CHIME/FRB Collaboration et al. 2025a). The first Outrigger, k’ni?atn k’l_stk’masqt (KKO),⁴⁶ is located in British Columbia, 66 km west of CHIME, and provides improved localizations of order $1''$ in R.A. (A. E. Lanman et al. 2024). The second CHIME Outrigger is located at the National Radio Astronomy Observatory in Green Bank, West Virginia, and together with the CHIME-KKO baseline, it can provide 50 mas by $20''$ localization capabilities (A. P. Curtin et al. 2025; S. E. Andrew et al. 2025 in preparation). The third and final CHIME Outrigger is located in Hat Creek, California, at the Hat Creek

⁴⁵ We colloquially refer to FRB 20250316A as RBFLOAT, for the Radio Brightest FLash Of All Time. We use “flash” to refer to perceived intensity (S/N), noting that there have been ~ 10 other FRBs detected in the CHIME/FRB side lobes of even higher fluence than FRB 20250316A (CHIME/FRB Collaboration et al. 2020b; H.-H. Lin et al. 2024).

⁴⁶ The name of the first Outrigger, k’ni?atn k’l_stk’masqt, was a generous gift from the Upper Similkameen Indian Band and means “a listening device for outer space.”

Table 1
FRB 20250316A Measured Radio Properties

Property	Value
R.A. (ICRS)	12 ^h 09 ^m 44 ^s .319
decl. (ICRS)	+58°50′56″.708
Error ellipse semimajor radius	$a = 68$ mas
Error ellipse semiminor radius	$b = 57$ mas
Error ellipse position angle	$\theta = -0.26$ east of north
Time of arrival (UTC)	2025-03-16 08:33:50.859038(3) ^a
DM	161.82(2) pc cm ⁻³
Peak flux density	1.2(1) kJy
Fluence	1.7(2) kJy ms ^b
Burst width (component 1)	0.0228(4) ms
Burst width (component 2)	0.226(3) ms
Scattering timescale 1	0.0851(6) ms ^c
Scattering timescale 2	0.405(1) ms ^c
Scattering frequency evolution 1	-4.47(2)
Scattering frequency evolution 2	-3.08(1)
Linear polarization fraction	0.9547(2)
RM	+16.79(85) rad m ⁻²

Notes. FRB 20250316A is a two-component burst, and we report the burst width and scattering timescale per component. Parenthetical numbers indicate uncertainties in the least-significant digits.

^a Topocentric at 400 MHz.

^b Fluence is band-averaged.

^c Referenced to 600 MHz.

Radio Observatory and provides the uv -coverage necessary for a full 2D localization of $\sim 50 \times 150$ mas. The full four-station (three Outriggers and the core CHIME telescope) array is still being commissioned, and its astrometric performance will be fully characterized in an upcoming work. Here we summarize our procedure for localizing this burst as well as a brief justification for the error bars reported.

We used `pyfx` (C. Leung et al. 2025) to obtain cross-correlated visibilities between station beams formed at CHIME and each Outtrigger site. VLBI fringes on FRB 20250316A were clearly detected with cross-correlation S/N exceeding 100 on all CHIME Outtrigger baselines. As described by S. Andrew & CHIME/FRB Collaboration (2025), the target visibilities were delay-referenced using the in-beam Radio Fundamental Catalog (RFC) calibrator RFC J1204+5202, located approximately 6° from the FRB (S. Andrew et al. 2025; L. Y. Petrov & Y. Y. Kovalev 2025).

Two main tests were performed to derive an error budget for this FRB localization. Similar to the test localizations presented by A. E. Lanman et al. (2024), the first was archival localizations of over 200 RFC calibrators and VLBI-localized pulsars with the full Outtrigger array to derive a representative error budget on each CHIME Outtrigger baseline as a function of cross-correlation S/N, bandwidth, and calibrator-target separation. For test localizations with similarly high S/N, bandwidth, and calibrator-target separations as FRB 20250316A, our rms error budgets on the CHIME-HCO and CHIME-GBO baselines were 57 mas and 68 mas, respectively. The second test was localizing all detected in-beam calibrators by phase-referencing delays to one another so that angular separations on the sky were maximized in our tests. We note that the delay offsets from our bootstrapping method were consistent with those obtained from our archival localizations under similar target-calibrator separations and at

lower cross-correlation S/N than observed in this data set. These calibrations provided the localization ellipse parameters given in Table 1: R.A. (ICRS) = 12^h09^m44^s.319, decl. (ICRS) = +58°50′56″.708, $a_{\text{err}} = 68$ mas, $b_{\text{err}} = 57$ mas, and $\theta = -0.26$ east of north.

This localization confirms the findings of C. Leung & CHIME/FRB Collaboration (2025) and M. Ng & CHIME/FRB Collaboration (2025) that FRB 20250316A is robustly associated with the nearby galaxy NGC 4141 in the vicinity of a star-forming clump (see Sections 5.1 and 5.4). We display the 1σ , 2σ , and 3σ localization ellipses on top of our MMT optical image (Section 3.2.1) in Figure 1. NGC 4141 has a Tully–Fisher distance of 37–44 Mpc (J. G. Sorce et al. 2014; R. B. Tully et al. 2016) and a redshift of $z \approx 0.0067$ (L. Connor et al. 2025).

3. Multiwavelength Follow-up

3.1. Radio

3.1.1. Radio Burst Monitoring

After the initial detection, FRB 20250316A was observed at high cadence as part of the HyperFlash project (PI: O. S. Ould-Boukattine), which monitors known FRB sources using a network of 25–32 m European radio telescopes with fluence sensitivities better than ~ 15 Jy ms. Observations are carried out on a best-effort basis, and, whenever possible, the telescopes observe simultaneously at complementary wavelengths. During this campaign, the position of FRB 20250316A was observed using telescopes at Westerbork (the Netherlands), Dwingeloo (the Netherlands), Stockert (Germany), Toruń (Poland), and Onsala (Sweden). A full description of the observing strategy is given by F. Kirsten et al. (2024). We also observed with the Nançay Radio Telescope (NRT; France) as part of the Extragalactic Coherent Light from Astrophysical Transients (ÉCLAT; PI: D. M. Hewitt) monitoring campaign. These observations used the Nançay Ultimate Pulsar Processing Instrument (G. Desvignes et al. 2011) and recorded data at a central observing frequency of 1.484 GHz, with 512 MHz of bandwidth.

FRB 20250316A was observed between 2025 March 16 (14 hr after the detection) and 2025 May 15 for a total nonoverlapping exposure at the L band of 244.06 hr and at the P band of 30.94 hr. The first ~ 120 hr of this campaign were summarized by O. S. Ould-Boukattine et al. (2025). There were no detections of bursts in this campaign. All telescopes would have been sensitive to bursts above 15 Jy ms, but, e.g., NRT observed for 13.69 hr and detected no bursts above 0.59 Jy ms.

3.1.2. Radio Continuum Imaging

We performed continuum radio follow-up observations using the European VLBI Network (EVN), the High Sensitivity Array (HSA), the Karl G. Jansky Very Large Array (VLA), and the upgraded Giant Metrewave Radio Telescope (uGMRT) to search for compact, persistent radio emission and characterize the radio environment surrounding FRB 20250316A. Full details regarding the individual observations and calibration are provided in Appendix B.

EVN and HSA. EVN observations were carried out on 2025 March 25 from 17:00 UTC to 05:00 (+1) UTC (ID: RL008; PI: M. Lazda). Observations were performed at a central

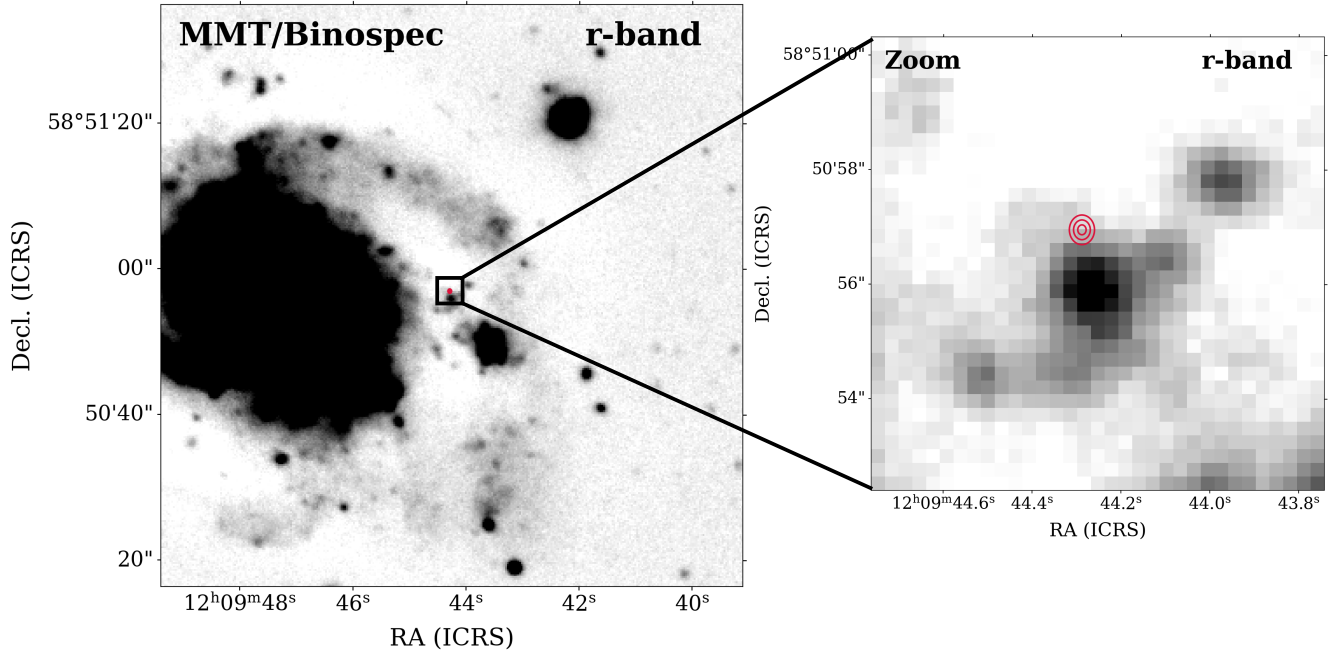


Figure 1. Left: linearly scaled MMT r -band image showing part of the host galaxy, NGC 4141, of FRB 20250316A with the CHIME Outrigger VLBI localization overlaid in red; the ellipse incorporates both positional and absolute astrometric tie uncertainties. The 3σ limiting magnitude of the image is $r \gtrsim 25.6$ mag (AB, corrected for Galactic extinction). The image is oriented north up and east left. Right: image zoomed in at the Outrigger position, $8'' \times 8''$, and additionally showing the 1σ , 2σ , and 3σ localization ellipses of FRB 20250316A.

frequency of 4.86 GHz, and data were recorded at a sampling rate of 4096 Mbps (512 MHz of bandwidth, full polarizations, 16 subbands, 32 MHz subband $^{-1}$). The integrated time resolution of the observations was set to 2 s sample $^{-1}$. The data were correlated at the Joint Institute for VLBI European Research Infrastructure Consortium using the Super FX Correlator (A. Keimpema et al. 2015).

HSA observations were carried out on 2025 April 1 from 02:30 UTC to 10:45 UTC with participation of all 10 standard VLBA dishes and the phased VLA in D-configuration (ID: B1327A; PI: M. Lazda). Observations were performed at a central frequency of 4.87 GHz, and data were recorded at a sampling rate of 4096 Mbps (512 MHz of bandwidth, full polarization, four subbands, 128 MHz subband $^{-1}$). The integrated time resolution of the observations was set to 2 s sample $^{-1}$. The data were correlated at Socorro using the DiFX correlator (A. T. Deller et al. 2007). Further details on phase calibration for both data sets can be found in Appendix B.

We identified no significant radio emission with either the HSA or EVN within $1''$ of the quoted localization region in Table 1, placing a 5σ upper limit on any compact, persistent radio emission of $\leq 22 \mu\text{Jy}$ and $\leq 46 \mu\text{Jy}$ with the HSA and EVN, respectively. Residual dirty images obtained with both VLBI arrays are provided in Appendix B.

VLA. We obtained multifrequency (3–27 GHz) VLA observations of the field of FRB 20250316A in the S , C , X , and K bands (central frequencies of 3.2, 6.1, 9.9, and 21.8 GHz, respectively) on 2025 April 4 and 2025 May 10 UTC (ID: 25A-434; PI: M. Lazda) while the VLA was in the D-configuration. We obtained a third epoch at the X band while the VLA was in the C-configuration on 2025 May 30. For observations at the C , X , and K bands, we utilized the 3 bit samplers with the full 4 GHz of bandwidth at the C and X bands and 8 GHz of bandwidth at the K band (excluding the

excision of edge channels and RFI). For the S band, we used the standard 8 bit samplers with ~ 2 GHz of bandwidth.

We processed and imaged the data using the standard VLA pipeline (version 6.6.1–17) as part of the Common Astronomy Software Applications (J. P. McMullin et al. 2007) software package. We performed bandpass and flux density calibration using NVSS J133108+303032 and complex gain calibration with NVSS J115324+493109, NVSS J121710+583526, and ICRF J121906.4+482956. We do not detect radio emission at the FRB location in the X - and K -band images, with 5σ rms values of 11 and $34.5 \mu\text{Jy}$, respectively. At the S and C bands, the lower angular resolution of the array in D-configuration is ill suited for probing compact radio emission associated with the FRB position: we instead detect extended radio emission coincident with the host galaxy, which we use to characterize the radio star formation rate (SFR) in Section 5.3. A subset of the radio images is provided in Appendix B.

uGMRT. We conducted uGMRT radio observations in Band 4 (550–750 MHz) and Band 5 (1260–1460 MHz) to search for any continuum radio emission associated with FRB 20250316A (ID: ddtC-430; PI: Y. Bhusare). A total of 8 hr were observed in Band 5 and 3 hr in Band 4. NVSS J133108+303032 was used as the flux density calibrator for both bands, while NVSS J131337+545824 and NVSS J120624+641337 were used as the complex gain calibrators for Band 5 and Band 4, respectively. The data were processed and imaged using the CAPTURE pipeline (R. Kale & C. H. Ishwara-Chandra 2020). We do not detect any continuum source at the target position above a 5σ significance threshold of $100 \mu\text{Jy}$ in Band 4 and $75 \mu\text{Jy}$ in Band 5. However, we detect some emission associated with the host galaxy in both bands. A summary table of all continuum radio observations is provided in Appendix B.

3.2. Optical

3.2.1. MMT

We obtained r -band imaging of the field of FRB 20250316A on 2025 March 23 (PI: J. Rastinejad; ID: UAO-G169-25A) with the Binospec optical spectrograph mounted on the 6.5 m MMT telescope atop Mount Hopkins, Arizona, for a total exposure time of 0.98 hr at ~ 8.23 days after the FRB detection (first reported by Y. Dong & CHIME/FRB Collaboration 2025). We reduced the images using the `POTPyRI` software package.⁴⁷ `POTPyRI` applies flat-field and bias calibration, performs absolute and relative alignment, and coadds the science frames into a single stack (Figure 1). We performed astrometric alignment relative to sources in common with the Gaia Data Release (DR) 3 catalog (Gaia Collaboration et al. 2023), which is well aligned to the ICRF (Gaia Collaboration et al. 2021, 2022) relative to the precision of the FRB localization. We will also note that as an additional check on the relative alignment between Gaia and ICRF coordinates, we cross-matched (with a search radius of 100 mas) 12 Gaia and RFC sources within a 1° patch centered at the FRB and found a median offset that was less than 1 mas (as expected).

The resulting solution for the relative alignment of our optical images to Gaia yielded astrometric uncertainties of $\Delta R.A. = 0''.053$ and $\Delta \text{decl.} = 0''.046$, which are added in quadrature to the localization ellipse parameters. With the photometric zero-point calibrated to PanSTARRS (H. A. Flewelling et al. 2020), there is no clear source at the Outrigger position to a 3σ limit of $r \gtrsim 25.6$ mag (hereafter, all quoted magnitudes are in the AB system and corrected for Galactic extinction in the direction of the FRB). We note that the FRB position is slightly to the north of an extended clump of emission (Figure 1), with a total magnitude of $r \approx 21.8$ mag ($M_r \approx -11.2$ mag at the adopted distance of NGC 4141, $d_L \approx 40$ Mpc).

To assess any variability at or near the FRB position, we acquired a second set of MMT r -band observations on UT 2025 March 24 (PI: Y. Dong; ID: UAO-G159-25A), 1.26 days after our initial observation for a total exposure of 0.98 hr. Performing digital image subtraction with `HOTPANTS` (A. Becker 2015), we do not detect any residual emission to a 3σ limit of $r \gtrsim 25.0$ mag, or $M_r \approx -8.0$ mag. We note that we can only comment on variability between these two epochs and are not sensitive to longer-timescale variability.

3.2.2. Gemini

Imaging. We imaged the field of FRB 20250316A with the Gemini Multi-Object Spectrograph (GMOS) mounted on the 8 m Gemini-North telescope on UT 2025 March 24 (PI: T. Eftekhari; ID: GN-2025A-LP-110) for a total exposure of 0.5 hr in the g band. As in the MMT imaging, we used `POTPyRI` to apply bias and flat-field corrections and to coadd the images. We carried out astrometric calibration using sources in common with the Gaia DR3 catalog, achieving a 1σ astrometric tie uncertainty of $\sim 0''.08$. We do not detect any optical emission coincident with the FRB localization to a 3σ point-source limiting magnitude of $g \gtrsim 23.7$ mag, as reported by S. Simha et al. (2025).

Spectroscopy. We obtained 8×900 s of long-slit optical spectroscopy of the localization region of FRB 20250316A

with GMOS on 2025 March 25 (PI: T. Eftekhari; ID: GN-2025A-LP-110). Observations were conducted using a $1''$ slit width, the B480 grating, and the GG455 blocking filter at central wavelengths of 640 and 650 nm. The resulting spectra covered a wavelength range of 4480–8560 Å. We oriented the slit at a position angle of 10.6° east of north to cover both the initial FRB Outrigger position (as reported by S. Andrew & CHIME/FRB Collaboration 2025) and the nearby clump of optical emission directly to the south of the FRB Outrigger position. We reduced and coadded the spectra using the `PypeIt` software package⁴⁸ (J. X. Prochaska et al. 2020). All frames were subject to basic image processing: bias subtraction, astrometric alignment, wavelength calibration, and flat-fielding to normalize pixel-to-pixel variation. We applied absolute flux calibration using spectrophotometric standard spectra. To avoid the masking of bright emission lines, the automatic cosmic-ray detection and masking was turned off.

We do not detect any spectral features at the FRB position but observe strong nebular emission ($H\beta$, $H\alpha$, and $[O\text{ III}]$) from the location of the nearby extended r -band emission detected in our MMT imaging with a common redshift of $z = 0.0065$. This is consistent with the emission originating from star formation within NGC 4141.

3.2.3. Keck Cosmic Web Imager

On 2025 March 22, 6 days after the FRB event, we observed the location of the FRB with the Keck Cosmic Web Imager (KCWI) integral field spectrograph (PI: T. Treu; Progid: U036). We used the “Small” slicer, which covers a field of view of $8'' \times 20''$ with the highest spatial resolution offered by the instrument ($0''.34 \text{ pixel}^{-1}$), and the BL and RL gratings on the blue and red arms ($R \approx 3600$ and $R > 2000$, respectively). We obtained a total of 2060 s on the blue arm (2×1030 s) and 1800 s on the red arm (6×300 s) on source without dithering. We also obtained off-source exposures of the same durations on a blank patch of sky offset by $30''$ from our initial pointing. To calibrate our exposures, we obtained the standard bias frames, ThAr comparison lamps, internal flat-fields, dome flat-fields, sky flat-fields, alignment frames, and standard-star exposures (CALSpec standard BD+54 1216; R. C. Bohlin et al. 2025).

The data were also reduced using the `PypeIt` reduction package. As mentioned in Section 3.2.2 for our Gemini spectroscopic data, our KCWI frames were first subject to basic image processing steps. However, as recommended by `PypeIt` documentation, in anticipation of coadding the individual exposures, spectral illumination correction was turned off. Then, one of the sky flats (dome flats) for the blue side (red side) was subsequently reduced as a science frame to provide relative scale correction in the coaddition step. The resulting 2D science spectra were coadded with the `pypeit_coadd_datacube` script to produce spectral data cubes. As the field of view was entirely within the disk of the host galaxy on the sky, each science frame was paired with one of the blank sky exposures to better subtract the sky emission. During coaddition, the standard-star data were also employed for flux calibration.

After reduction and fluxing, we corrected the astrometric solution of the red and blue cubes. Since no obvious point

⁴⁷ <https://github.com/CIERA-Transients/POTPyRI>

⁴⁸ <https://github.com/pypeit/PypeIt> (version 1.17; `kcwi_dec_2024` branch).

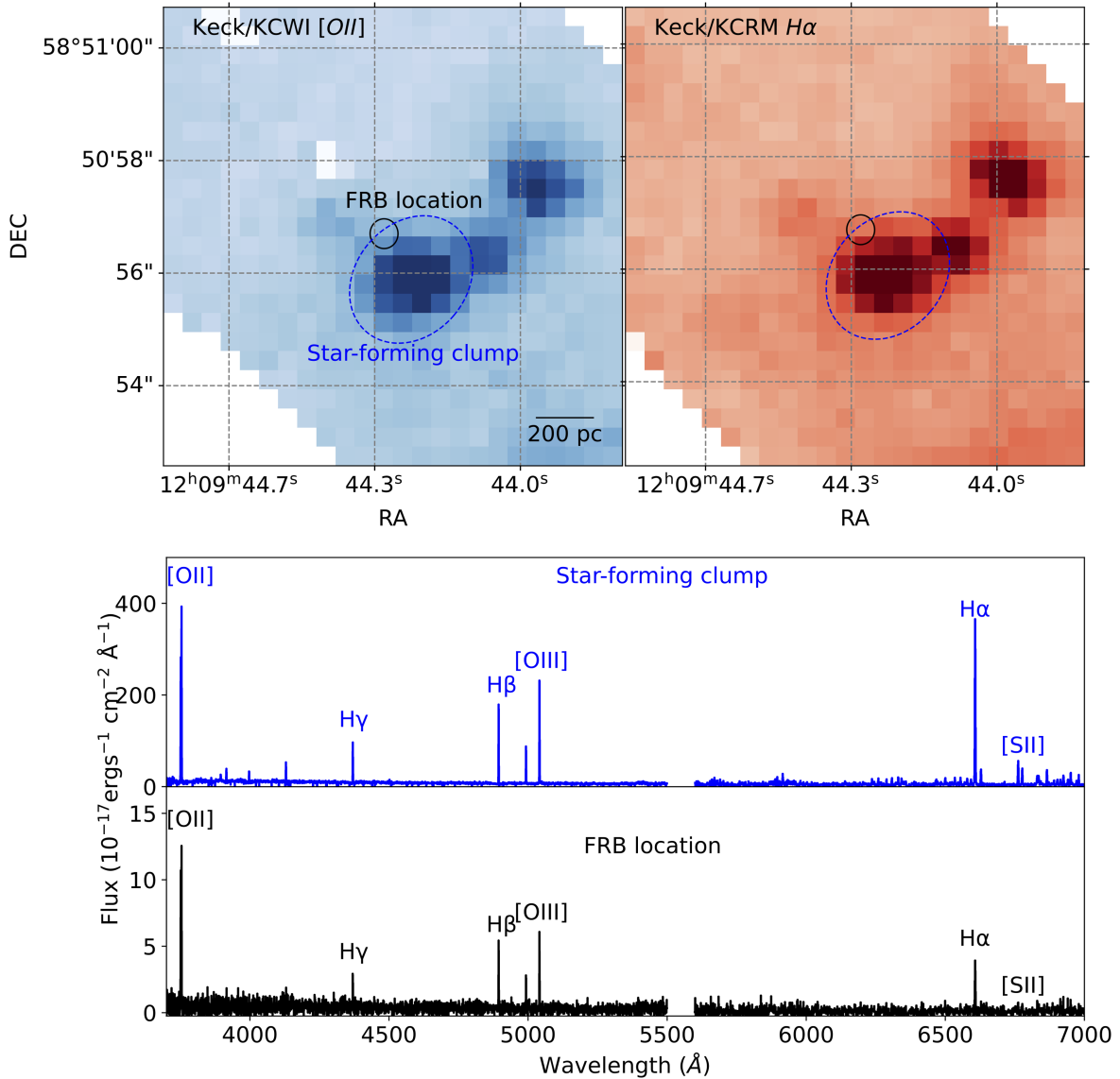


Figure 2. KCWI narrowband images of the burst location. The top panels show [O II] 3726, 3729 Å and Hα images extracted from the coadded cubes of the blue and red arms of KCWI, respectively. The solid black ellipse shows the 2σ localization region of the FRB, placing its center at 190 pc projected separation ($0''.9$ angular offset) from the emission peak of the nearby star-forming region, which is marked by the dashed blue ellipse. The middle panel shows the combined blue and red side 1D spectrum of the star-forming clump extracted within the dashed ellipse. The bottom panel shows the spectrum extracted from the FRB localization ellipse. The gap in the spectra between 5500 and 5600 Å masks out the region where the dichroic splits the blue and red light. Both spectra show narrow nebular emission features, and we do not see any transient features at the location of the FRB.

source was identified on the cube, we attempted to align the centroids of the three line-emitting clumps in Figure 2 with the corresponding clumps in our deep MMT *r*-band image (shown in the right panel of Figure 1). To this end, narrowband maps of Hα and the [O II] $\lambda\lambda 3726, 3729$ doublet were generated, and the sources were characterized through *Photutils* image segmentation. Simultaneously, sources were identified in the MMT image. Offsets between the source centroids in the KCWI and MMT images were computed. The median value of these offsets was applied to the KCWI world coordinate system (WCS) solution to produce the final, astrometrically calibrated datacube. No rotation correction was applied as both the data cubes and the MMT images have north and east directions aligned with the image axes from their respective reduction packages. Also, no higher-order WCS corrections were applied on account of the sparsity of sources to accurately derive these terms. The uncertainty in this

astrometric correction was estimated with the standard deviation of the individual offsets to the three clumps: $0''.1$ for both the blue- and red-arm cubes. Our analyses with the KCWI data (i.e., as described in Section 5.4) incorporate this astrometric uncertainty by adding it in quadrature with the FRB localization uncertainty and the MMT-Gaia astrometric tie-in uncertainties.

Preliminary examination of the cubes revealed strong emission features, including the [O II] 3726, 3729 Å doublet and Hα, from clumps in the host galaxy interstellar medium (ISM). The top panels of Figure 2 show the clumps in close proximity to the FRB location. We compared these relatively compact features to our MMT imaging to calibrate the cube astrometry since the KCWI data do not cover any known star or point source in the field of view. Similar to the MMT imaging, we do not observe any obvious point source at the location of the FRB itself. Further analysis of the KCWI data,

including 1D extraction in and around the FRB localization, is presented in Section 5.4.

3.3. X-Ray

Upon receiving FRB 20250316A’s VOEvent from CHIME/FRB, the Neil Gehrels Swift Observatory repointed to the position reported in the VOEvent.⁴⁹ However, FRB 20250316A did not end up in the field of view of Swift/XRT X-ray Telescope (XRT) as the initial VOEvent position was incorrect.⁵⁰ The true position was outside of the reported 1σ uncertainty region and hence was not in the FOV of Swift/XRT. We repointed Swift/XRT via target-of-opportunity (ToO) request once we had a refined baseband position for the burst; we began observing on 2025 March 16 at 21:10 UTC, 12.6 hr after the time of arrival (ToA) of the burst (PI: A. Tohuvavohu), and observed the position for 6.2 ks. An additional Swift ToO observation (PI: E. Troja) of 10.3 ks took place about 1 week after the event. Preliminary analyses of the Swift observations (target ID 19620) have been reported elsewhere (E. Troja et al. 2025; Y. J. Yang et al. 2025), but the observations have been reanalyzed with the updated position in this work. These led to 0.5–10.0 keV upper limits on the unabsorbed flux of 7×10^{-14} and 1×10^{-13} erg cm⁻² s⁻¹ for the two observations, respectively, assuming an isotropic emission with a $\Gamma = 2$ power-law spectrum, absorbed by an $N_{\text{H}} = 1.4 \times 10^{20}$ cm⁻² neutral hydrogen column. This neutral hydrogen column corresponds to the Galactic expectation (HI4PI Collaboration et al. 2016) and assumes negligible X-ray absorption local to the source.

Follow-up observations by the Einstein Probe (EP) showed evidence of X-ray variability at the position consistent with FRB 20250316A between 2025 March 18 and 21 (H. Sun et al. 2025a). The subsequent follow-up Chandra/High Resolution Camera observation (PI: H. Sun), with its subarcsecond spatial resolution capability, combined with the updated subarcsecond localization from CHIME/FRB Outriggers (S. Andrew & CHIME/FRB Collaboration 2025), ruled out a physical association between the EP-detected variable X-ray source and FRB 20250316A (H. Sun et al. 2025b). Follow-up ToO observations (PI: A. B. Pearlman) with the Neutron Star Interior Composition Explorer (NICER) between 2025 March 18 and 21 (ObsIDs 861701010[1–4]; ~ 6.7 ks) yielded 3σ persistent X-ray-absorbed 0.5–10.0 keV flux upper limits in the range $(0.07\text{--}3) \times 10^{-12}$ erg cm⁻² s⁻¹ with similar spectral parameters assumed above (A. B. Pearlman et al. 2025a).

4. Radio Burst Analysis

4.1. Morphology

FRB 20250316A exhibits a scattered two-component structure at the top of the observed band, transitioning to a single scattered component at lower frequencies. Using DM_phase (A. Seymour et al. 2019), we find an incoherent structure optimizing DM of 161.82 ± 0.02 pc cm⁻³. As shown in Figure 3, the burst peak displays substantial drift in time as a function of frequency, consistent with a frequency-dependent

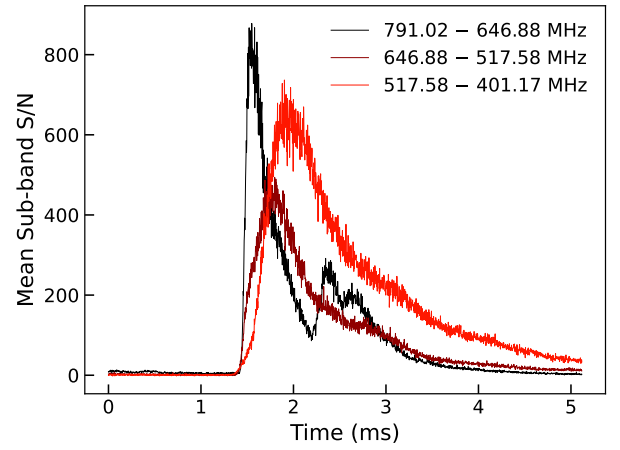


Figure 3. S/N of FRB 20250316A averaged over three frequency subbands and at the 2.56 μ s time resolution native to the raw voltage data.

rise time expected for multiple scattering screens as seen by F. Kirsten et al. (2022).

A pulse-broadening function associated with multiple screens is not a model currently available within the burst-modeling software typically used for CHIME/FRB data, fitburst (E. Fonseca et al. 2024). To capture this behavior, we define a new burst model from two Gaussian components convolved with two thin screen scattering kernels and fit it to the profile using the Bayesian Inference Library (Bilby; G. Ashton et al. 2019). The intrinsic components are centered at t_1 and t_2 and characterized by 1σ widths w_1 and w_2 . The scattering kernels are each the canonical one-sided exponential decay with $1/e$ widths τ_1 and τ_2 referenced to 600 MHz that scale with frequency following α_1 and α_2 . Further fit details are discussed in Appendix C, and the best-fit parameters are listed in Table 1.

4.2. Polarimetry

We applied the CHIME/FRB polarization pipeline (for details, see R. Mckinven et al. 2021) to the beamformed baseband data for FRB 20250316A to study its polarization properties. The total intensity waterfall plot, linear and circular polarization fractions, and polarization angle (PA) profile are shown in Figure 4. We measure an average linear polarization fraction $L/I = \sqrt{Q^2 + U^2}/I = 0.9547 \pm 0.0002$ across the burst. Note here that the small uncertainty is derived only from the Stokes Q and U spectra, and it does not account for leakage into Stokes V , which may add additional uncertainty on the L/I at the roughly percent level. No circular polarization is detected above the expected instrumental polarization level. The linear polarization fraction remains constant across 400–800 MHz, and we find no evidence for beam depolarization in the signal. The frequency-averaged PA profile displays a complex morphology with a maximum variation of $\sim 20^\circ$ – 30° across the burst profile. Given the high S/N of this burst, we split the burst into 16 frequency bands and measure the PA profile as a function of decreasing frequency, as shown in Figure 5. We see that the PA profile has larger variations at the top of the CHIME/FRB band and flattens near the bottom as it becomes increasingly scatter-broadened. Even at the lower frequencies measured by CHIME/FRB, the leading edge of the burst retains much of the PA variability before it becomes flat in the scattering tail. This PA profile flattening with

⁴⁹ This was achieved through the “continuous commanding” capability that can achieve 10 s latency response time on-orbit to unscheduled ToO requests received on the ground (A. Tohuvavohu et al. 2024).

⁵⁰ The VOEvent position was reported based on an incorrect assignment of the beam with the highest-S/N detection (see Section 2.1).

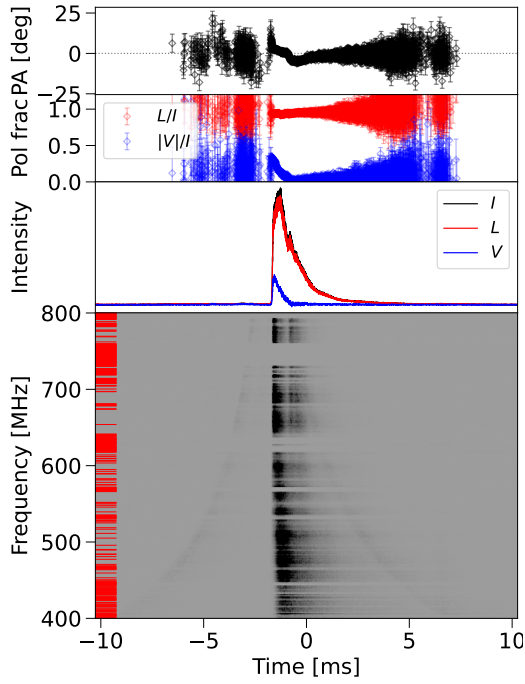


Figure 4. Bottom: total intensity waterfall dedispersed to the structure-optimized DM of $161.82 \pm 0.02 \text{ pc cm}^{-3}$ and temporal profiles of Stokes I (black line), $L = \sqrt{Q^2 + U^2}$ (red line), V (blue line), linear polarization fraction (L/I ; red circles), circular polarization fraction ($|V|/I$; blue circles), and PA (black circles). Channels masked out due to RFI are highlighted by red streaks on the left-hand side of the total intensity waterfall. The preceding and subsequent parabolic sweeps are artifacts due to “spectral ghosts” related to the instrumental signal chain. Top: all points plotted on the L/I , $|V|/I$, and PA profiles exceed a linearly polarized S/N of 5.

frequency is a known effect in pulsars (e.g., X. H. Li & J. L. Han 2003; P. F. Wang et al. 2023; W. C. Jing et al. 2025); however, this is the first reported instance for FRBs. Physically, this flattening is thought to arise from the averaging of PAs in a given time bin within the scattering tail, where signals from different pulse phases (and hence with different PAs) have become mixed.

To measure the Faraday RM, we employ the RM-synthesis algorithm (B. J. Burn 1966; M. A. Brentjens & A. G. de Bruyn 2005) as implemented by R. Mckinven et al. (2021) and search for peaks in the Faraday dispersion function exceeding a linearly polarized S/N of 6. We observe an RM of $\text{RM}_{\text{obs}} = 16.7853 \text{ rad m}^{-2}$ with a statistical error of $0.0003 \text{ rad m}^{-2}$. In this case, the systematic error in RM measurements with CHIME/FRB (0.85 rad m^{-2} , as measured using multipepoch polarimetric monitoring of Crab giant pulses; R. Mckinven et al. 2023) dominates the statistical error, so we quote an observed RM of $\text{RM}_{\text{obs}} = 16.79 \pm 0.85 \text{ rad m}^{-2}$. The Galactic RM contribution toward FRB 20250316A is $\text{RM}_{\text{gal}} = 17 \pm 4 \text{ rad m}^{-2}$ (S. Hutschenreuter et al. 2024). Assuming negligible RM contributions from the intergalactic medium and Earth’s ionosphere and converting to the rest frame of the source, we constrain the host galaxy contribution to the RM to be $\text{RM}_{\text{host}} = 0 \pm 4 \text{ rad m}^{-2}$. However, the Galactic RM map by S. Hutschenreuter et al. (2024) does not constrain RM variations on scales smaller than $\sim 1 \text{ deg}^2$, which can change the RM_{gal} estimate by up to $\sim 40 \text{ rad m}^{-2}$ even away from the Galactic plane (A. Pandhi et al. 2025). This effectively places larger (unknown) uncertainties on our RM_{host} estimate, and we cannot conclusively determine whether FRB 20250316A

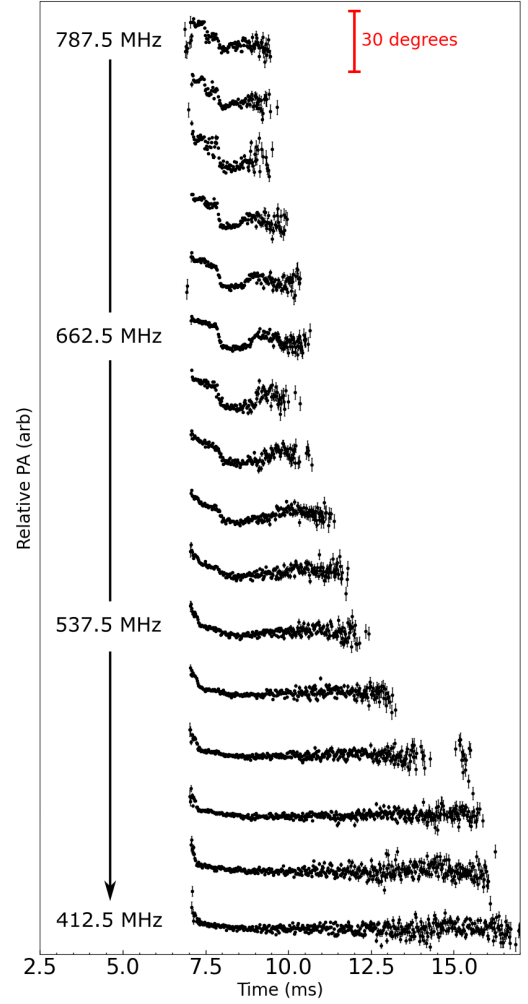


Figure 5. PA profile of FRB 20250316A as a function of frequency over 400–800 MHz. The y-axis scale is arbitrary, and a red marker is used to indicate PA variation on a 30° scale. The central frequencies of some frequency subbands are indicated on the left as a guide.

originates from a weak magnetoionic environment (i.e., one with $|\text{RM}_{\text{host}}| \approx 0 \text{ rad m}^{-2}$). Using our estimates of $\text{DM}_{\text{host}} = 60 \text{ pc cm}^{-3}$ (assuming a conservative uncertainty of 20 pc cm^{-3} ; see Section 5.4.4) and $\text{RM}_{\text{host}} = 0 \pm 4 \text{ rad m}^{-2}$, we calculate $\langle B_{\parallel, \text{host}} \rangle = 4 \pm 100 \text{ nG}$, noting again that our uncertainties may be underestimated.

Compared to the average nonrepeating FRB population (A. Pandhi et al. 2024), FRB 20250316A stands out in a number of ways: (i) it is more highly linearly polarized than average, (ii) it undergoes a larger PA swing than most nonrepeating FRBs, and (iii) it has the lowest RM contribution from its host galaxy (consistent with 0 rad m^{-2}) of any polarized nonrepeater currently observed by CHIME/FRB.

4.3. Scintillation

We perform a cursory scintillation analysis using the methodology outlined by K. Nimmo et al. (2025). We find convincing evidence for at least one scale of scintillation, with a decorrelation bandwidth of approximately $\nu_{\text{DC}} = 14 \pm 4 \text{ kHz}$ at 600 MHz, as shown in Figure 6. We observed the scintillation to have a low modulation index consistent with interference effects from the interplay between two scattering surfaces (K. Nimmo

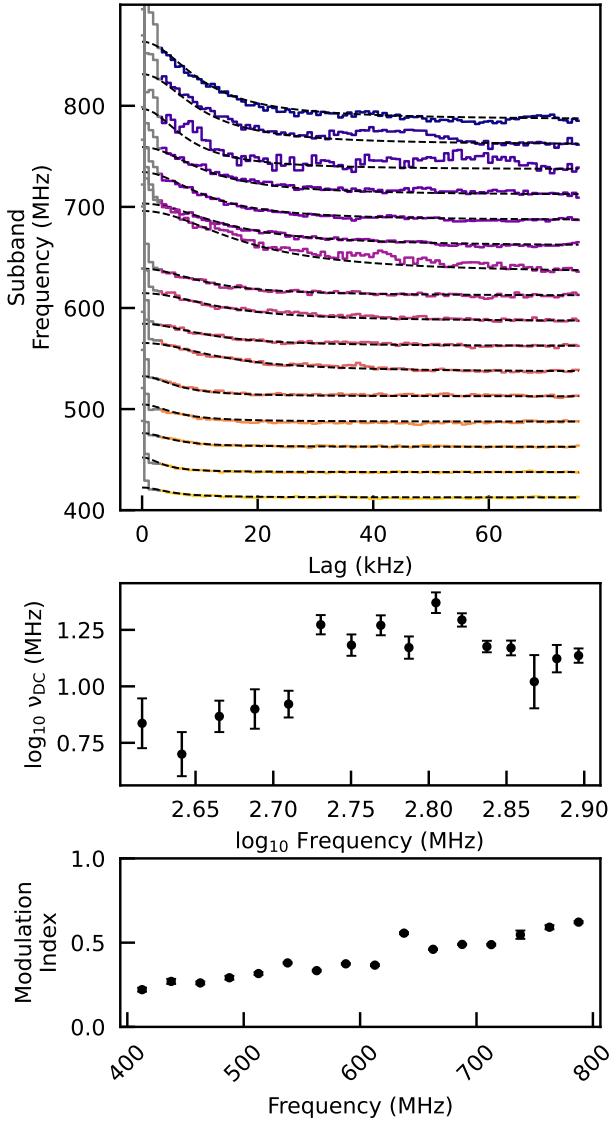


Figure 6. Top: autocorrelations of equal-bandwidth subband spectra and corresponding Lorentzian fits to observed scintillation. Gray regions denote data associated with distinct spectral structures on a separate scale that are excluded from the scintillation fit discussed in this work. Middle: decorrelation bandwidth (ν_{DC}) as a function of frequency. Bottom: modulation index associated with the scintillation decorrelation bandwidth seen in the top panel.

et al. 2025; S. Pradeep E. T. et al. 2025), in broad agreement with the two scattering screens inferred from the scattering tail and scattering-induced rise time in the burst morphology. We highlight that the observed ν_{DC} appears to flatten toward higher frequencies, contrary to the expectation of S. Pradeep E. T. et al. (2025) for evolution to steepen at higher frequencies. The extent to which this flattening deviates from theory, the impact of instrumental artifacts on the spectrum, a treatment of finer-scale spectral structures, and tests of consistency between spectral and temporal scattering effects will be considered more exhaustively in a future work.

As in previous studies (M. W. Sammons et al. 2023; K. Nimmo et al. 2025), the scintillation and scattering times for separate screens may be used to constrain their geometries. S. Pradeep E. T. et al. (2025) show that as stronger scattering increases the size of the illuminated screens (L_1 and L_2) relative to the distance between them ($D_{1,2}$), the modulation

index of the relatively broad scale of scintillation decreases following

$$m = \frac{1}{\sqrt{1 + \frac{\pi^2}{4^3} \left(\frac{L_1 L_2}{\lambda D_{1,2}} \right)^2}}, \quad (1)$$

where λ is the wavelength. Commensurate with this change in modulation index, the relatively broad scale of scintillation associated with a screen at D_1 is expected to widen following

$$\nu_{DC} = \frac{c D_1}{\pi L_1^2} \sqrt{1 + \frac{\pi^2}{4^3} \left(\frac{L_1 L_2}{\lambda D_{1,2}} \right)^2}. \quad (2)$$

Given our modulation index of $m = 0.4$, we can use the observed scattering times to constrain the minimum distance between these two screens for some reasonable assumption of their effective distances ($D_s D_{sf}/D_f$, the angular diameter distances to screen, between screen, and the FRB and to the FRB, respectively). We assume that one screen is located at the peak of turbulence strength along this line of sight at a distance $D_{MW} = 0.25$ kpc inferred from the ne2001 profile (J. M. Cordes & T. J. W. Lazio 2002; S. K. Ocker et al. 2022), where this source is at a high Galactic latitude of $b = 57.46^\circ$. As a result, the distance between the screens must be greater than 1 Mpc for all second screens at effective distances greater than 3 pc. We therefore conclude that one of the screens must be extragalactic.

The product of separations of extragalactic and Galactic screens from the host and observer, respectively, may then be constrained, following the updated method outlined by S. Pradeep E. T. et al. (2025), using the scintillation and the larger of the two scattering times. We constrain the product of the angular diameter distances between the observer and Galactic scattering screen (D_g) and the source and host galaxy scattering screen ($D_{x,s}$) to be $D_g D_{x,s} \lesssim 0.015(4)$ kpc². We describe this constraint conservatively here as a limit but highlight that in reality, it should be an equality provided the systematics are well understood. This is orders of magnitude more constraining than typical (M. W. Sammons et al. 2023), due primarily to the proximity of this source. Assuming again that our Galactic scattering screen lies at the peak of turbulence strength for this sight line of 250 pc, the extragalactic scattering screen must be within approximately 60 ± 20 pc of the source, the tightest constraint yet.

4.4. Limits on FRB Repetition Rate

CHIME/FRB's 269.77 hr of exposure toward FRB 20250316A is distributed in 8–11 minute⁵¹ intervals over our 6 yr of operation. CHIME/FRB has not detected any other candidate bursts with $S/N \geq 8.5$ and a position and DM consistent with FRB 20250316A (within 10 pc cm^{-3} and an angular separation of 1°). CHIME/FRB has some sensitivity and much more exposure to very bright bursts in our side lobes, where we have detected at least 10 FRBs with FRB 20250316A-level fluences many degrees off meridian (CHIME/FRB Collaboration et al. 2020a; H.-H. Lin et al. 2024). Thus, we also search positions that are consistent with

⁵¹ The daily transit time has steadily increased as the precession of the Earth moves the source transit more centrally through its corresponding row of formed beams.

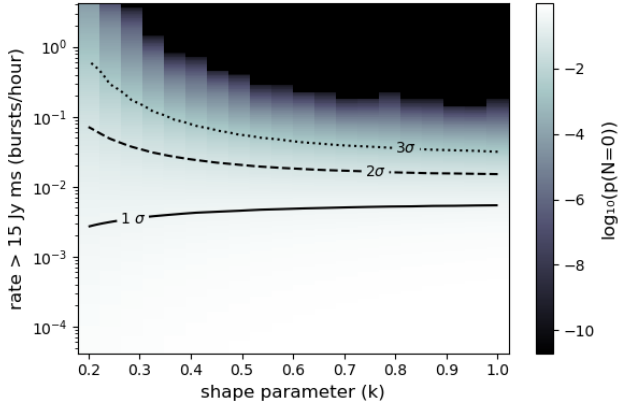


Figure 7. Probability of detecting no bursts in the HyperFlash observations (color map) as a function of assumed shape parameter (x-axis) and burst rate above 15 Jy ms (y-axis). Contours corresponding to the 1σ , 2σ , and 3σ confidence upper limits are superimposed.

the time-dependent apparent position of FRB 20250316A as it transits through the side lobes up to 60° from the telescope’s meridian but find no convincing burst candidates.

The HyperFlash observations (Section 3.1.1, the timeline of which is visualized in Appendix A) targeted the source shortly after discovery and began with a particularly constraining 33 hr L -band exposure just 14 hr after the initial detection of FRB 20250316A. No bursts were detected. Repeater bursts are known to cluster in time, with waiting distributions well described by a Weibull distribution (N. Oppermann et al. 2018; but see also D. C. Good et al. 2023). The Weibull distribution describes the intervals between events, and it is a generalization of the Poisson distribution described by two parameters. In this analysis, we adopt the parameterization of N. Oppermann et al. (2018) such that the first Weibull parameter, $r \in \mathbb{R}^+$, can still be interpreted as a rate, and the additional shape parameter $k \in \mathbb{R}^+$ describes the extent of clustering. When $k = 1$, the Weibull distribution reduces to the Poissonian case, and when $k < 1$, small intervals are favored compared to the Poissonian case.

Using the HyperFlash L -band observations, in Figure 7, we show the region of parameter space that can be ruled out at different confidence levels given our observations. This is done via simulation: for different values of k and r , we randomly sample waiting times from the corresponding Weibull distribution and check how frequently zero bursts occur during any of our observing windows. Assuming Poisson statistics ($k = 1$), we can rule out rates greater than 2.4×10^{-2} bursts hr^{-1} above the sensitivity threshold, 15 Jy ms, at the 99.7% level.

When additionally considering CHIME/FRB’s 269.77 hr of exposure over the 6 yr prior to the discovery of FRB 20250316A, Poisson rates above 1.5×10^{-2} bursts hr^{-1} are ruled out at the 99.7% confidence level above 15 Jy ms. Here, these observations are combined assuming that all telescopes, including CHIME, are sensitive above 15 Jy ms and simply adding the total nonoverlapping exposure time. These rate upper limits are only valid under the assumption that the source was in an active state with a constant rate for the entirety of the observations, which we caution is a much more reasonable assumption for the HyperFlash observations that took place in the weeks following our detection than it is for the 6 previous yr of CHIME/FRB observations.

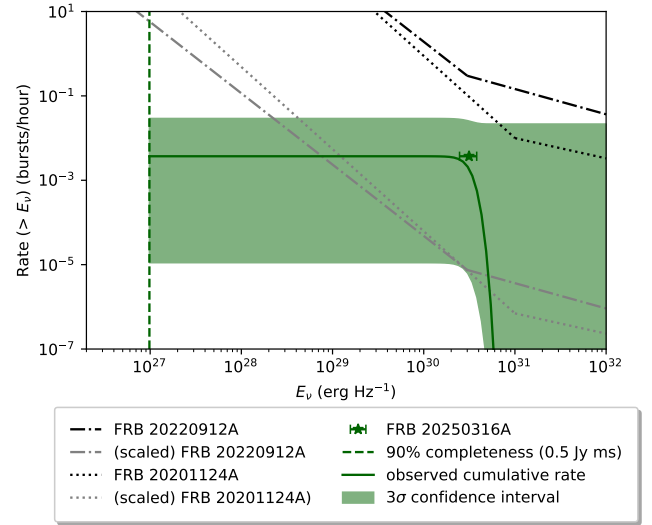


Figure 8. Cumulative rate as a function of spectral energy. The empirical/observed cumulative rate for FRB 20250316A is shown as a solid green line. We show the 99.7% confidence intervals around the observed cumulative rate assuming Poisson statistics (green region). The single observed burst from FRB 20250316A is marked at its measured spectral energy (green star). Our sensitivity threshold (0.5 Jy ms) is shown with a green vertical dashed line. For comparison, we show the observed best-fit spectral energy functions for FRB 20201124A (F. Kirsten et al. 2024) and FRB 20220912A (O. S. Ould-Boukattine et al. 2024) with black dotted and dotted–dashed lines, respectively. Even scaling these observed overall rates down orders of magnitude, essentially as low as possible without making the observation of the first burst improbable (gray dotted and dotted–dashed lines for scaled-down cumulative rate distributions of FRB 20201124A and FRB 20220912A, respectively), reveals a significant dearth of lower-energy bursts compared to the expected rates, illustrating the tension between this burst and well-studied repeating FRBs.

4.5. Burst Energy Distribution Constraints

The more puzzling aspect of FRB 20250316A, if it were to be a repeater, is its high S/N, which is a reflection of its relative proximity. Given its measured fluence of 1.7(2) kJy ms and NGC 4141’s distance of ~ 40 Mpc, we derive a burst spectral energy of $(3.1 \pm 0.7) \times 10^{30}$ erg Hz^{-1} .

Known repeaters are observed to have power-law fluence distributions, with higher repetition rates at lower fluence. If FRB 20250316A were a repeater, CHIME/FRB should be sensitive to those lower-fluence bursts, and a lack of detection allows us to constrain the likely burst luminosity function. Assuming a cumulative rate distribution as a function of burst spectral energy with a power-law index of $\alpha = -1.5$, the probability that we detect a burst of this spectral energy and nothing less energetic, considering our fluence threshold, is less than 2×10^{-6} (4.7 σ Gaussian equivalent) for this source alone (i.e., even maximizing among all possible overall burst rates). If one controls for the family wise error rate using the Bonferroni correction (O. J. Dunn 1961) considering our (~ 100) total confirmed repeaters, this observation is inconsistent with an $\alpha = -1.5$ power-law index at a 3.7 σ Gaussian equivalent level ($p < 2 \times 10^{-4}$). Indeed, even assuming that every unique FRB source that we have detected to date is a repeater (using a trial factor extrapolated from the source count at the cutoff of CHIME/FRB’s Second Catalog to ~ 5000), there is a $< 1\%$ chance of such an observation per CHIME/FRB experiment, i.e., in the first 5000 detected FRB sources. This tension is illustrated in the empirical cumulative rate as a function of spectral energy in Figure 8, where even scaling the overall rate of the repeaters down orders of magnitude,

essentially as low as would still statistically allow for the detection of the first burst, reveals a significant dearth of lower-energy bursts.

Assuming the measured power-law indices of known repeaters FRB 20220912A and FRB 20201124A, -1.69 and -1.94 , respectively, relevant for spectral energies below 3×10^{30} and 1×10^{31} erg Hz $^{-1}$, respectively (F. Kirsten et al. 2024; O. S. Ould-Boukattine et al. 2024), the probability of detecting only one burst with spectral energy $(3.1 \pm 0.7) \times 10^{30}$ erg Hz $^{-1}$ and no lower-energy bursts above our 1×10^{27} erg Hz $^{-1}$ sensitivity threshold decreases by 1 and 2 orders of magnitude (to 5.1σ and 5.4σ Gaussian equivalent). Considering the nondetection by FAST (H. Qian et al. 2025) in the week following FRB 20250316A’s detection, this probability decreases by an additional order of magnitude (5.2σ , 6.1σ assuming $\Gamma = -1.5$, -1.96 , respectively). However, this number should be considered with the caveat that both the HyperFLASH and FAST observations took place at a higher radio observing frequency, and while FRBs discovered in the CHIME band are commonly detected at ~ 1400 MHz (L band), ultimately, the average repeater burst spectral energy distribution is not well characterized. Similarly, while the FAST observations took place at the L band promptly after established source activity, the comparatively short exposure time of 13 hr in six exposures spread over 1 week suggests that the constraining power on the rate will be dominated by the assumed clustering, which is not accounted for in this probability.

4.6. V/V_{\max} Analysis

V/V_{\max} serves as a useful statistic to highlight the uniqueness of FRB 20250316A. V/V_{\max} is defined as the comoving volume interior to a source’s distance, divided by the comoving volume interior to the maximal distance at which that source could be detected ($V/V_{\max} = D_c^3(z)/D_c^3(z_{\max})$; M. S. Longair & P. A. G. Scheuer 1970). For a survey of sources distributed uniformly in comoving space, which is complete above some threshold, this statistic is also expected to be uniformly distributed between 0 and 1. For the case of FRBs, $D_c(z_{\max})$ corresponds to the distance where the fluence threshold of detection ($F_{\nu, \text{thresh}}$) corresponds to the energy of the burst E following (J. P. Macquart & R. Ekers 2018)

$$E = \frac{4\pi d_L^2(z) \Delta\nu F_{\nu, \text{thresh}} \sqrt{w_{\text{eff}}(z)}}{(1+z)^{2+\beta}}, \quad (3)$$

where β is the spectral index, d_L is the luminosity distance, and $\Delta\nu$ is the burst bandwidth. We include an additional factor representing the relative change in burst width as a function of redshift ($w_{\text{eff}}(z)$) to capture how increased width from DM and cosmological time dilation reduce the S/N of a detection at a given fluence, following the formalism in J. M. Cordes & M. A. McLaughlin (2003),

$$w_{\text{eff}} = \frac{\sqrt{(w_m(1+z))^2 + w_{\text{DM}(z)}^2 + \tau^2}}{w_m}, \quad (4)$$

where w_m is the width measured in the observed burst, $(1+z)$ is the cosmological time dilation factor, $w_{\text{DM}(z)}$ is the contribution to the observed width from dispersive smearing as a function of redshift, and τ is an additional scattering

component from intervening structures at larger distances that we do not take to have a strict functional form with redshift.

To calculate V/V_{\max} , we use FRB 20250316A’s measured burst fluence of 1700 Jy ms, a fluence threshold of 0.5 Jy ms (see Appendix A), a fiducial burst bandwidth of 1 GHz, and a spectral index of $\beta = -1.39$ (K. Shin et al. 2023) and assume a Planck cosmology (Planck Collaboration et al. 2020). To scale the width, we use a fiducial measured width of $w_m = 1$ ms; calculate the dispersive smearing at the central observing frequency of CHIME, 600 MHz, using the 24.4 kHz channels in the CHIME/FRB detection system (CHIME/FRB Collaboration et al. 2021); and include a flat $\tau = 1$ ms scattering time as a conservative estimate of the contribution to scattering from intervening structures (J. X. Prochaska et al. 2019). To maintain this conservative approach, we deliberately overestimate the excess DM acquired at greater distances by using the 3σ excess from the Macquart relation (J. P. Macquart et al. 2020) for the highest DM variance scenario ($F \approx 0.25$) seen among the CAMELS suite of simulations (I. Medlock et al. 2024). Under these assumptions, FRB 20250316A is detectable out to $z = 0.42$ ($d_L = 2370$ Mpc), at which point the burst has accrued an additional 555 pc cm $^{-3}$ of DM and 1 ms of additional scattering and is 61% of its original energy following the spectral index and emission in a higher-frequency rest frame. This maximum redshift yields $V/V_{\max} = 1.4 \times 10^{-5}$. To contextualize the scale of this value, if we integrate the comoving volume over the whole sky out to infinite redshift, it converges to a value of ≈ 3800 Gpc 3 . Taking this value as V_{\max} , $V/V_{\max} \leq 1.4 \times 10^{-5}$ is only possible for sources interior to $z \geq 0.079$ ($D_c = 340$ Mpc); for all other sources, there is insufficient volume in the observable Universe. We highlight that several other nearby, high-fluence bursts have been detected by CHIME/FRB in its broad side lobes (H.-H. Lin et al. 2024). In these cases, however, the associated detection thresholds are much higher than for FRB 20250316A, substantially reducing their expected V/V_{\max} values.

Using the above method, we can compare this result to V/V_{\max} for the 3375 one-off FRB sources with measured fluence in the Second CHIME/FRB Catalog (CHIME/FRB Collaboration et al. 2025b). To estimate the true redshift of each FRB, we translate the observed DM using the $p(z|DM)$ relationship modeled by K. Shin et al. (2023). The resulting V/V_{\max} values are shown in Figure 9. Notably, the observed bursts do not populate to the $V/V_{\max} = 1/3375 = 10^{-3.53}$ level as expected for a uniform population of sources in comoving space, which should yield a correspondingly uniform distribution of V/V_{\max} values. We expect this is due to instrumental selection bias introduced when high-S/N events are flagged as RFI. If we assume that the selection-corrected distribution is uniform, a fiducial CHIME-like sample of 5000⁵² FRBs has a 7.0% chance of containing a V/V_{\max} on this scale; therefore, FRB 20250316A is potentially consistent with the observed population of one-off CHIME bursts.

In the nearby Universe, where cosmological populations do not undergo significant redshift evolution of their ensemble density and luminosity functions, the assumption of a uniform V/V_{\max} distribution is well justified. Conversely, as the next generation of FRB surveys like the Canadian Hydrogen

⁵² This burst was observed subsequent to the cutoff date of CHIME/FRB’s Second Catalog and therefore belongs to a larger sample whose size we estimate through extrapolation.

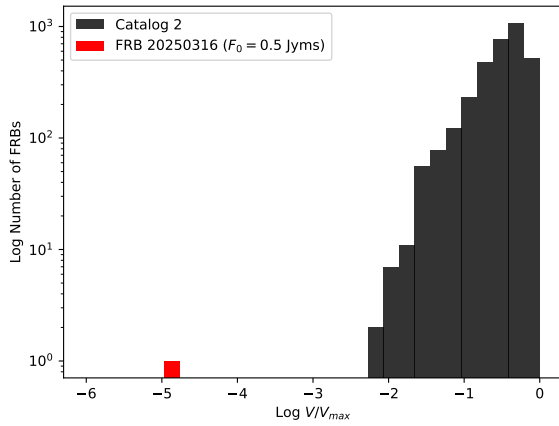


Figure 9. Comparison of the V/V_{\max} statistic for FRB 20250316A, in red, against a simulated distribution for the one-off bursts in the Second CHIME/FRB Catalog, using DM as a proxy for distance under the z -DM distribution derived by K. Shin et al. (2023).

Observatory and Radio Transient Detector and the Deep Synoptic Array 2000 (G. Hallinan et al. 2019; K. Vanderlinde et al. 2019) begin to detect more distant FRBs, the evolution of these properties is expected to impact the observed V/V_{\max} distributions. If FRBs trace star formation, as expected for a young magnetar progenitor model, the increase in cosmic star formation toward redshift 2 will bias observations toward higher V/V_{\max} values. However, progenitor channels involving long delay time distributions, such as neutron star mergers (M. Zevin et al. 2022), are expected to have a flatter redshift distribution between $z = 0$ and 2, yielding a more uniform distribution of V/V_{\max} . Astrophysically, the methodology therefore represents a useful tool for understanding FRBs and should be considered in the future.

However, the traditional V/V_{\max} estimator for truncated luminosity functions lacks a strong statistical foundation, with no theorems proving its unbiasedness or asymptotic normality, requiring arbitrary binning, and often having poor performance in reproducing known luminosity functions (e.g., T. T. Takeuchi et al. 2000; E. D. Feigelson & G. J. Babu 2012; Z. Yuan and J. Wang 2013; A. K. Weigel et al. 2016). In future work estimating the luminosity functions of populations of FRBs, it is more appropriate to utilize the Lynden-Bell–Woodroffe–Wang estimator (D. Lynden-Bell 1971; M. Woodroffe 1985; M.-C. Wang et al. 1986; V. Petrosian 1992).

5. Host Galaxy NGC 4141 and FRB Environment

5.1. Host Identification and Galactocentric Offset

We used the VLBI localization to associate a host candidate for FRB 20250316A using the Probabilistic Association of Transients to their Hosts (PATH) analysis, as described by K. Aggarwal et al. (2021). We identified host candidates using galaxy angular sizes and magnitudes from the DECaLS DR10 imaging catalog (A. Dey et al. 2019). FRB 20250316A is located within ~ 0.5 of NGC 4141. However, the imaging catalog also identifies star-forming regions within $\sim 40''$ from the galactic center of NGC 4141 as individual objects. We therefore use `photutils` to estimate the half-light radius of NGC 4141 and update the candidate list by removing these regions. We assume an exponential offset prior and a prior probability of an unseen host, $P(U|x)$, of 0.10 (B. C. Andersen et al. 2025, in preparation). The PATH analysis identifies NGC

4141 as the top candidate for the host of FRB 20250316A with a posterior probability, $P(O|x)$, of 99.95%.

From our MMT imaging (Section 3.2.1), we use `SExtractor` (E. Bertin & S. Arnouts 1996) to derive a light-weighted center for NGC 4141 of R.A. (ICRS) = $12^{\text{h}}09^{\text{m}}47^{\text{s}}.347$ and decl. (ICRS) = $58^{\circ}50'56.841''$. Incorporating the FRB positional, host positional, and astrometric tie uncertainties, we calculate a projected offset between the FRB and the host center of $23.''50 \pm 0.''11$ or 4.49 ± 0.02 kpc at 40 Mpc.⁵³

5.2. Limits on Emission at FRB Location

Radio. Our continuum radio observations (Section 3.1.2 and Appendix B) identified no evidence of compact radio emission associated with the FRB position, placing a 5σ upper limit on any associated counterpart of $\leq 22 \mu\text{Jy}$ at 4.87 GHz and $\leq 11 \mu\text{Jy}$ at 9.9 GHz. At a distance of 40 Mpc, this corresponds to an upper limit on the specific luminosity of $L_{4.93 \text{ GHz}} \leq 4.2 \times 10^{25} \text{ erg s}^{-1} \text{ Hz}^{-1}$ and $L_{9.9 \text{ GHz}} \leq 2.1 \times 10^{25} \text{ erg s}^{-1} \text{ Hz}^{-1}$. Previous limits reported using archival VLA data performed at the X band placed a 5σ upper limit on any associated compact radio emission of $4.8 \times 10^{25} \text{ erg s}^{-1} \text{ Hz}^{-1}$ (W. W. Golay et al. 2025). Interferometric measurements performed using eMERLIN achieved an upper limit of $2.2 \times 10^{26} \text{ erg s}^{-1} \text{ Hz}^{-1}$ (G. Bruni et al. 2025a). A summary of upper limits on any persistent radio counterpart is provided in Table 3 in Appendix B.

Optical. We can also place constraints on transient optical emission prior to and immediately following the FRB. Prior to the FRB, we use historical exposures of this field with the 0.76 m Katzman Automatic Imaging Telescope (KAIT) at Lick Observatory (A. V. Filippenko et al. 2001) and the Coddlenham Observatory, which have a cadence of ~ 10 exposures yr^{-1} in 2001–2009 and 3 exposures yr^{-1} thereafter. There is no evidence for pointlike optical transient emission down to $M_{\text{clear}} \approx -13.5$ mag (1σ). These exposures are deep enough to detect luminous optical transients including core-collapse supernovae (CCSNe) and Type Ia supernovae (SNe) as well as optical transients associated with the final stages of stellar evolution in some massive stars (such as those reported by A. Pastorello et al. 2007). However, the observing cadences of both KAIT and the Coddlenham Observatory are sensitive to only half of each year of observation, allowing for the possibility that a weeks-long optical transient was simply missed. We expect that the observations would have been sensitive to typical 1–2 month old SNe had one occurred in the gaps between observations.

From our MMT imaging (Section 3.2), we detect no apparent unresolved optical emission at the FRB position to $r \gtrsim 25.6$ mag or $M_r \gtrsim -7.4$ mag. At the distance to NGC 4141 ($d \approx 40$ Mpc), this upper limit corresponds to an in-band luminosity of $1.9 \times 10^{38} \text{ erg s}^{-1}$. With this limit, a comparison to single-star evolutionary tracks (J. Choi et al. 2016) suggests that we can rule out the presence of massive main-sequence stars with initial masses $\gtrsim 40 M_{\odot}$, as well as evolved stars (i.e., red supergiants) with masses $\gtrsim 20 M_{\odot}$. Similarly, our limit can be used to place constraints on slowly evolving transients. For instance, we can rule out the presence of a young ($\lesssim 1$ yr) CCSN at the FRB position based on CCSN light curves (W. V. Jacobson-Galán et al. 2025). After the FRB occurred,

⁵³ This value is the straight-line distance between the center of the FRB localization and the host galaxy with 1σ uncertainties added in quadrature.

our MMT imaging indicates no new point source relative to archival imaging (taken in 2016–2017) and no transient emission to $M_r \approx -8$ mag on timescales of ~ 8.2 – 9.5 days after the FRB. This limit is sensitive to rapidly evolving transients such as gamma-ray burst afterglows, kilonovae, and fast blue optical transients (V. A. Villar et al. 2017; A. Y. Q. Ho et al. 2023).

If the FRB progenitor is a magnetar formed through the core collapse of a massive star, a past SN or historical optical transient may be spatially coincident with the FRB. To this end, we search for cataloged optical transients from the Transient Name Server at the FRB position following the method described in Y. Dong et al. (2025). We find no significant associations within the 5σ localization uncertainty of FRB 20250316A. Within NGC 4141, there are two reported Type II SNe, SN 2008X and SN 2009E (T. Boles 2008; A. Pastorello et al. 2012), which lie 31.5 and 41.2 away from FRB 20250316A, respectively. More recently, an unclassified optical transient, AT 2025erx, was discovered in the same galaxy prior to the FRB on 2025 January 17 (I. Andreoni & A. Palmese 2025) and lies 57.7 away from the FRB. Given such large positional separations, we conclude that a physical association with either the SNe or the optical transient is ruled out.

5.3. Radio SFR

Following J. Greiner et al. (2016), we estimate the radio-inferred SFR, $\text{SFR}_{\text{radio}}$, of NGC 4141 to compare to the optically inferred value. The radio-inferred SFR is given by

$$\text{SFR}_{\text{radio}} = 0.059 M_{\odot} \text{ yr}^{-1} F_{\nu, \mu\text{Jy}} d_{L, \text{Gpc}}^2 \nu_{\text{GHz}}^{\gamma} (1+z)^{(\gamma-1)}, \quad (5)$$

where F_{ν} is the observed flux density at a frequency ν and d_L is the luminosity distance at a redshift z . We adopt $\gamma = -0.75$ (J. J. Condon 1992) for the spectral index, as the measured flux becomes increasingly resolved out at higher frequencies, leading to unreliable estimates of the source flux and hence spectral index. Using the VLA S-band flux density (see Table 3 in Appendix B), we infer a 3.2 GHz radio SFR for the host galaxy of $\text{SFR}_{\text{radio}} = 0.2 M_{\odot} \text{ yr}^{-1}$. This is comparable to, albeit lower than, the SFR as inferred from $\text{H}\alpha$ of $0.6 M_{\odot} \text{ yr}^{-1}$ (L. J. Kewley et al. 2005). This minor discrepancy may be attributed to variations in the radio-infrared correlation across spiral arms and interarm regions due to differences in the ISM properties that complicate the use of nonthermal radio emission as an SFR indicator (e.g., G. Dumas et al. 2011). Alternatively, the larger $\text{H}\alpha$ SFR may point to a recent enhancement in star formation, given the typical timescales of 10 Myr probed by line indicators compared to the 100 Myr timescales associated with nonthermal synchrotron emission.

5.4. Local Environment

The coadded KCWI data cubes reveal several compact star-forming clumps with strong nebular emission features. Indeed, consistent with the MMT imaging, the FRB localization centroid is offset from the centroid of the nearest star-forming clump by 0.9 ± 0.1 ,⁵⁴ which corresponds to 190 ± 20 pc in projected separation at the host distance. In Figure 2, we show

the combined spectrum (from the red and blue arms) of the clump extracted within a $1.5''$ aperture. Also shown is the spectrum of the region extracted from an elliptical aperture corresponding to the 2σ localization region of the FRB. Comparing the two spectra, there is no strong evidence of any emission lines associated with a potential transient, i.e., no significant difference in line widths or the detection of features atypical of galactic nebular emission.

In addition to investigating the presence of transient optical emission, we leverage our spectroscopic data cubes to characterize the local gas environment in the vicinity of the FRB. To this end, we produce emission line maps from the cube by extracting spectral slabs covering the emission lines of interest and then fitting a flat continuum model with Gaussian line profiles for individual lines for each spaxel. Instead of fitting the entire wavelength range, we divide our cubes into three slabs covering (1) the $[\text{O II}]$ 3726, 3729 Å doublet; (2) $\text{H}\beta$ and the $[\text{O III}]$ 4959, 5007 Å doublet; and (3) $\text{H}\alpha$, the $[\text{N II}]$ 6548, 6584 Å doublet, and the $[\text{S II}]$ 6718, 6733 Å doublet. This simplifies our computation and also avoids the need for reprojecting the blue cube to the red WCS system, as there is a slight offset between the cubes. With the line fluxes extracted at each spaxel (0.34×0.34), we employ standard emission line diagnostics (that we shall describe below) to infer the gas properties of the host ISM.

5.4.1. ISM Ionization State

The Baldwin–Phillip–Terelevich (BPT) diagram (J. A. Baldwin et al. 1981) is a line-ratio diagnostic of excitation mechanisms driving gas ionization of ISM gas. Since we detect the four lines $\text{H}\alpha$, $[\text{N II}]$ 6584, $[\text{O III}]$ 5007, and $\text{H}\beta$, we can place the emitting clump near the FRB location on the diagram to ascertain the nature of the radiation. We do not perform a per-spaxel BPT analysis, since there is a very slight offset between the red- and blue-arm data cubes that precludes a one-to-one mapping between the spaxels of the two cubes. Instead, we opt to extract the line fluxes from the spectra of the clump and the FRB location (middle and bottom panels of Figure 2) and use these to determine the gas properties at the two locations.

Figure 10 shows the BPT diagram with our data points overlaid. Both the clump and the FRB location are consistent with gas ionization from star-forming activity within H II regions.

5.4.2. SFR and Dust Extinction

The $\text{H}\alpha$ emission flux is a well-known indicator of present SFR through the R. C. Kennicutt (1998) relation. It is strongly detected throughout the cube footprint (see Section 5.4.4 for the spatially resolved emission map). However, one must account for dust extinction from the Milky Way and the host galaxy ISM before converting the line flux to the SFR. To correct the photometry for Galactic extinction, we query the IRSA dust extinction database⁵⁵ at the FRB position and find $E(B - V) = 0.05$ (E. F. Schlafly & D. P. Finkbeiner 2011). We rely on the measured flux ratio $\text{H}\alpha/\text{H}\beta$ to first estimate the dust extinction and subsequently correct the $\text{H}\alpha$ flux. We assume $R_V = 3.1$ and subsequently apply the extinction correction to the line fluxes. Then, to correct for the host

⁵⁴ As mentioned in Section 3.2.3, the localization error ellipses include the radio localization error, the astrometric uncertainty in the MMT-Gaia tie-in, and the astrometric uncertainty in aligning the KCWI cubes to the MMT image.

⁵⁵ <https://irsa.ipac.caltech.edu/applications/DUST/>

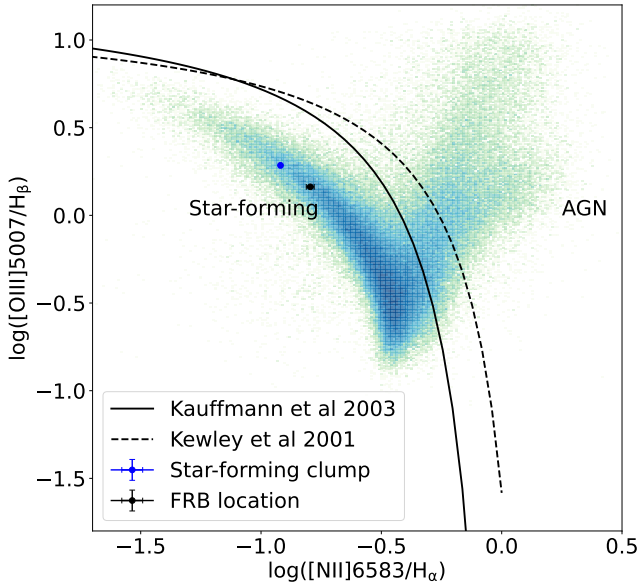


Figure 10. BPT diagram showing the clump and emission at the FRB location compared to the field galaxies (blue–green color map). Both locations show ionization consistent with star-forming activity, i.e., to the left of the G. Kauffmann et al. (2003) demarcation (black solid line) and the L. J. Kewley et al. (2001) demarcation (black dashed line).

galaxy dust extinction, we assume that the intrinsic ratio of $H\alpha/H\beta$ fluxes is 2.87 (D. E. Osterbrock & G. J. Ferland 2006) and attribute the deviation from this ratio to dust extinction, allowing us to compute the visual extinction A_V from the spectra (we also assume $R_V = 3.1$ here). To this end, we assume the G23 extinction model (K. D. Gordon et al. 2023) from the `dust_extinction` Python package (K. Gordon 2024). After dereddening, we apply the Kennicutt relation and multiply the result by 0.63 (C. Conroy et al. 2009) to report the SFR with the G. Chabrier (2003) initial mass function. The error is largely from the scatter in the Kennicutt relation (30%). As in the case of the BPT diagram, we do not provide maps of either star formation or dust extinction for the entire cube footprint due to the slight offset between the red and blue cubes. We again adopt the spectra extracted at the FRB location and the star-forming clump and tabulate our measurements in Table 2. We estimate that the star-forming clump is roughly producing $2.42 \times 10^{-2} M_\odot \text{ yr}^{-1}$.

5.4.3. ISM Metallicity

Of the various probes of ISM metallicity, the flux ratio R_{23} is known to have the least scatter (0.14 dex; T. Nagao et al. 2006; K. Nakajima et al. 2022), where

$$R_{23} = \frac{[\text{O II}] 3729 + [\text{O III}] 4959 + [\text{O III}] 5007}{H\beta}. \quad (6)$$

However, converting R_{23} to metallicity requires an additional line diagnostic, as it is double-valued; i.e., both low- and high-metallicity gas can produce similar values of R_{23} . Therefore, we show our maps of R_{23} and the flux ratio $[\text{N II}] 6584/H\alpha$ in the left and middle panels of Figure 11. Indeed, despite the noisier $[\text{N II}] 6584/H\alpha$ map, we note that most of the spaxels show that the flux ratio is $\gtrsim 0.1$, thus implying a metallicity $\log(Z/Z_\odot) > -0.5$ (K. Nakajima et al. 2022). Subsequently, we invert R_{23} in the high-metallicity regime to map $\log(Z/Z_\odot)$, shown in the right panel of Figure 11. The

Table 2

Dust Extinction and the SFR of the Host Galaxy in the Vicinity of the FRB

Location	A_V (mag)	SFR ($10^{-4} M_\odot \text{ yr}^{-1}$)
Star-forming clump	1.48 ± 0.02	242 ± 7
FRB location	0.32 ± 0.09	1.4 ± 0.4

Note. We note here that the reported error in A_V is purely from propagating the line flux measurement uncertainties and do not include the systematic error in assuming the G23 dust extinction model.

FRB location exhibits a weakly subsolar metallicity. This is consistent with the distribution of metallicity estimated by K. Sharma et al. (2024) for their host galaxy sample. We recognize that their measurements are for global host properties; thus, more integral field unit (IFU) data on nearby FRB hosts are necessary to determine the distribution of the ISM metallicity of FRB environments.

5.4.4. ISM Electron Density

The $[\text{O II}] 3726, 3729 \text{ \AA}$ doublet is collisionally excited, and the line flux ratio $[\text{O II}] 3729/[\text{O II}] 3726$ can serve as a probe of the ISM gas density assuming a typical ISM temperature ($\sim 10^4 \text{ K}$; D. E. Osterbrock & G. J. Ferland 2006). A similar analysis can be performed using the $[\text{S II}] 6717, 6731 \text{ \AA}$ doublet, but we opt to use $[\text{O II}]$, as it has much higher detection S/N throughout our data. We employ the line fluxes extracted on a per-spaxel basis (as described previously) to generate a map of the flux ratio over our full KCWI footprint. We only estimate the ratio in spaxels where the combined $[\text{O II}]$ doublet emission is detected at a significant level (3σ) over the background noise. To select these pixels, we first extract a narrowband image encompassing the wavelength range of the combined $[\text{O II}]$ doublet emission ($3746\text{--}3760 \text{ \AA}$). Then, we sigma-clip iteratively to identify the background spaxels and estimate the spaxel-to-spaxel standard deviation in flux. Finally, we select spaxels for our ratio estimation by requiring their flux to be above the 3σ background limit. In addition to the flux selection above, we also require that the line flux ratios only be estimated where both emission lines have been fit with a Gaussian with positive amplitude.

The left panel of Figure 12 shows the $[\text{O II}]$ doublet emission line ratio for our footprint. Two spaxels coincide with the 2σ localization region of the FRB (see left panel of Figure 12). Both the top and bottom spaxels indicate a flux ratio between 1.3 and 1.4, which could correspond to an electron density of $\sim 100 \text{ cm}^{-3}$. However, we estimate a standard error of ~ 0.2 for both spaxels (middle panel of Figure 12). The error is estimated by propagating the curve-fitting error for the two emission lines. Thus, the flux ratios of both spaxels could very well be $\gtrsim 1.45$, at the low-density limit for the line ratio ($\lesssim 1 \text{ e}^- \text{ cm}^{-3}$). Thus, while it appears that the electron density could be enhanced at the FRB location, we cannot claim a statistically significant detection of overdensity. The right panel of Figure 12 shows a histogram of flux-ratio measurements for all colored spaxels in the left panel. Most spaxels show a doublet ratio at or beyond the low-density limit. It is therefore possible that the ISM at the FRB location is also at similarly low density.

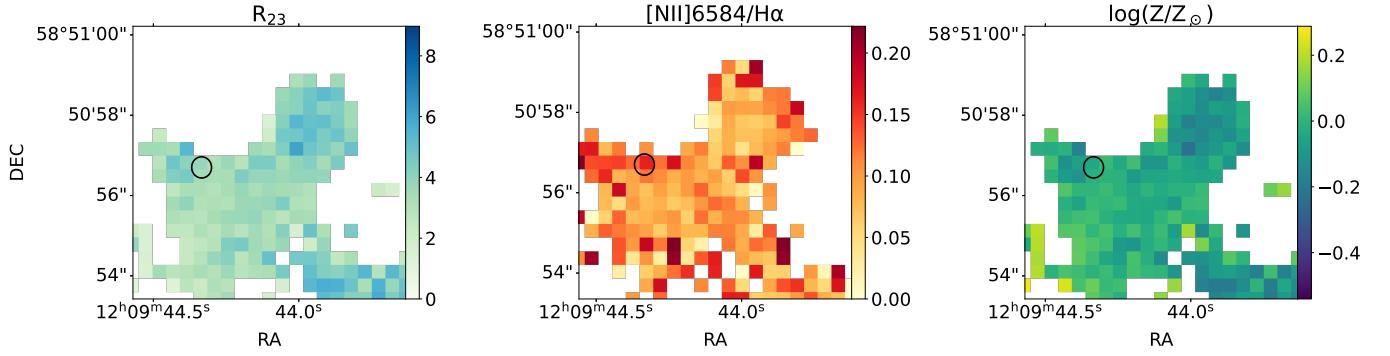


Figure 11. Strong-line metallicity diagnostics. Left: a map of R_{23} computed from the blue-arm data cube of KCWI. Middle: the $[\text{N II}] 6584/\text{H}\alpha$ flux ratio estimated from the red-arm data cube. Given that most spaxels near the FRB location show $[\text{N II}] 6584/\text{H}\alpha > 0.1$, we can safely assume that the metallicity is higher than 8.1 and thus break the degeneracy in R_{23} . Right: subsequently, we can invert the best-fit R_{23} - $\log(Z/Z_{\odot})$ relation on the high-metallicity branch of the curve to produce a metallicity map near the FRB (2σ localization, shown by the black ellipse). We note that the FRB environment’s metallicity is only weakly subsolar.

5.4.5. $DM_{\text{host,ISM}}$

In addition to assessing the electron density of the ISM from the doublet, we also leverage the $\text{H}\alpha$ emission measure ($\text{EM}_{\text{H}\alpha}$) to constrain the DM contribution from the host ISM. This method was first described in the context of pulsars in the Milky Way (R. J. Reynolds 1977) but was subsequently adopted by the FRB community (J. M. Cordes et al. 2016; S. P. Tendulkar et al. 2017; L. Bernales-Cortes et al. 2025) to derive empirical upper bounds on $DM_{\text{host,ISM}}$. Similar to our $[\text{O II}]$ analysis, we start with the spaxel-by-spaxel $\text{H}\alpha$ line flux estimate from our fits to the data. Here too, we restrict our analysis to spaxels that correspond to $\text{H}\alpha$ emission above the 3σ background threshold (wavelength range 6602–6612 Å). The $DM_{\text{host,ISM}}$ estimate from $\text{EM}_{\text{H}\alpha}$ is given by

$$DM_{\text{host,ISM}} = 387 \text{ pc cm}^{-3} \left(\frac{\text{EM}_{\text{H}\alpha}}{600 \text{ pc cm}^{-6}} \right)^{0.5} \times \left(\frac{L}{1 \text{ kpc}} \right)^{0.5} \left(\frac{F}{1} \right)^{0.5}, \quad (7)$$

where $F = 4f_{\text{ff}}/\zeta(1 + \epsilon^2)$ is a term that describes the properties of the emitting $\text{H}\alpha$ clouds and encompasses cloud properties such as the volume filling factor of emitting clouds (f_{ff}), turbulence-based fractional density variation in each cloud (ϵ), and density fluctuation between individual clouds (ζ) (J. M. Cordes et al. 2016). However, most FRB studies choose the value of $F = 1$ (the latest being L. Bernales-Cortes et al. 2025), which shall be our assumption as well. L is the column length of the emitting gas that the FRB traverses. We compute the $\text{H}\alpha$ surface brightness (in photon flux per unit solid angle measured in rayleighs; I_{R}) from our red-arm data cube and convert this to an emission-measure map using the equation $\text{EM}_{\text{H}\alpha} = 2.75 \text{ pc cm}^{-6} T_4^{0.9} I_{\text{R}}$ (R. J. Reynolds 1977). Here, T_4 is the gas temperature in units of 10^4 K. In the absence of accurate temperature diagnostics, we assume $T_4 = 1$, following the references mentioned above. Figure 13 shows our $\text{EM}_{\text{H}\alpha}$ map without any host galaxy dust extinction correction applied. Within the 2σ localization region, $\text{EM} = 282\text{--}987 \text{ pc cm}^{-6}$. The range of the EM arises from the surface brightness variation across the two pixels spanned by the localization ellipse. From Table 2, we can apply the estimated dust correction at the FRB location. Again, as done in Section 5.4.2, we use the extinction

model from K. D. Gordon et al. (2023) and $R_V = 3.1$ and estimate that the intrinsic $\text{H}\alpha$ surface brightness at the FRB location is 6% higher than the observed value, i.e., $\text{EM}_{\text{dereddened}} = 300\text{--}1050 \text{ pc cm}^{-6}$. This implies $DM_{\text{host,ISM}} = 61\text{--}115 \text{ pc cm}^{-3} (L/50 \text{ pc})^{0.5}$ at the FRB location. We choose 50 pc as a representative length scale here but emphasize that L is not known a priori.

One could, however, place constraints on L using DM budget arguments. Accounting for the DM from all other foreground components (the Milky Way, cosmic web, and host galaxy halo), one can place bounds on $DM_{\text{host,ISM}}$, which subsequently constrains L . Using models of the Milky Way ISM and halo (J. M. Cordes & T. J. W. Lazio 2002; J. X. Prochaska & Y. Zheng 2019; A. M. Cook et al. 2023), we can estimate that the Milky Way contribution to the FRB DM is $\sim 70 \text{ pc cm}^{-3}$. If all of the remaining 90 pc cm^{-3} were attributed to the ISM alone, the gas column length allowed by our $\text{EM}_{\text{H}\alpha}$ -based $DM_{\text{host,ISM}}$ estimate is 30–110 pc. Stricter bounds can be placed by accounting for the host halo and the foreground cosmic web. The stellar mass of the host is estimated to be $1.7 \times 10^9 M_{\odot}$ in the NASA/IPAC Extragalactic Database (NED) Local Volume sample⁵⁶ (D. O. Cook et al. 2023). Assuming the stellar-to-halo mass ratio of B. P. Moster et al. (2013) and applying the modified Navarro–Frenk–White profile halo gas model prescribed by J. X. Prochaska & Y. Zheng (2019; profile parameters $\alpha = 2$, $y_0 = 2$, $f_{\text{hot}} = 0.75$ extending to two virial radii), roughly 20 pc cm^{-3} can be attributed to the host halo. The cosmic web could contribute another 6 pc cm^{-3} to the DM budget (Y. Huang et al. 2025). Thus, if only 64 pc cm^{-3} arise from the host ISM, the gas column further reduces to 17–60 pc. Thus, we can conclude that the FRB is not deeply embedded in any $\text{H}\alpha$ -emitting gas region. Interestingly, the scintillation and scattering properties of the burst (Section 4.3) indicate a small separation ($\lesssim 60 \text{ pc}$) between the dominant scattering screen in the host and the FRB source. This coincidence suggests that the same $\text{H}\alpha$ -emitting gas region could also be responsible for the large-scale scattering (τ_2) observed in the burst profile.

We must further stress an important point: our KCWI data are seeing-limited. The star-forming clump is roughly $1.2''$ in diameter, comparable to the point-spread function size at the $\text{H}\alpha$ wavelength ($\sim 0.6''$ FWHM, estimated from our standard-

⁵⁶ We converted the NED estimate to the Chabrier initial mass function by dividing the listed value by 1.7.

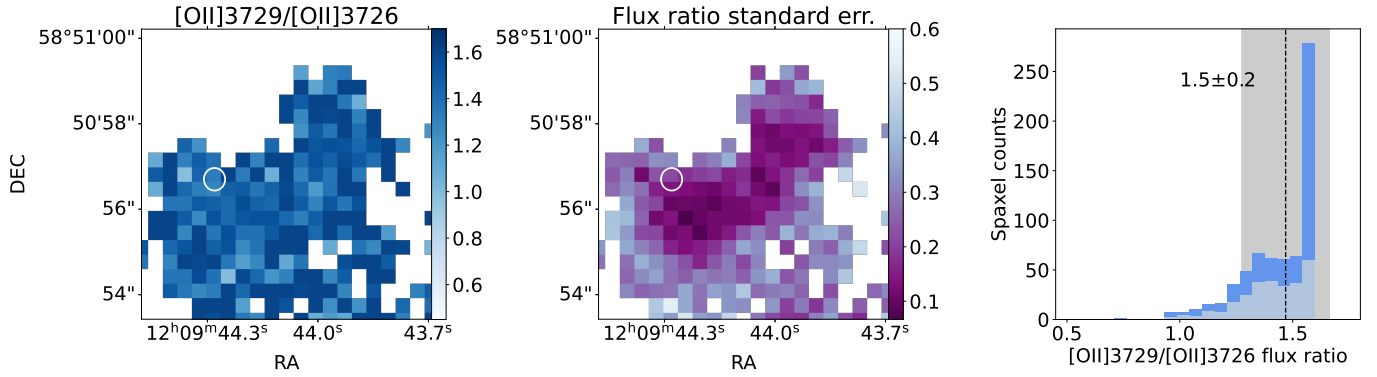


Figure 12. Left: [O II] 3729/[O II] 3726 line-ratio map over the KCWI footprint. The flux ratios are only computed where the combined [O II] doublet emission is over the 3σ limit set by the background and where the line fluxes are measured (i.e., positive-amplitude Gaussian fit to the emission line). Other spaxels are blanked out. The 2σ FRB localization is marked by the white ellipse. Middle: the per-spaxel error in the flux-ratio measurement estimated from propagating the curve-fitting errors. Right: a histogram of line-ratio values from all the colored spaxels in the left frame (deep blue). The median value is 1.5 with a standard deviation of 0.2, although the distribution is clearly non-Gaussian, and most spaxels have a line ratio of 1.6. If we limit the histogram to spaxels where the flux error is below 0.25 (i.e., the blue-green regions in the middle panel), then the peak at 1.6 is no longer as prominent, but most spaxels still have a flux ratio consistent with low-density gas ($\lesssim 1 \text{ e}^- \text{ cm}^{-3}$). The FRB line ratio at the FRB location could be slightly lower, implying an enhanced density, but our measurement errors preclude a definitive gas-density estimate.

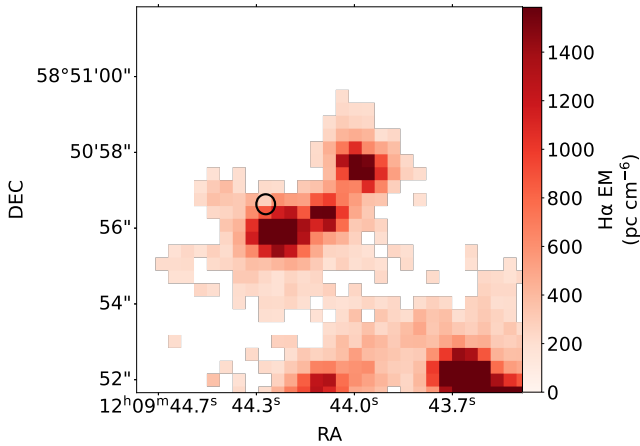


Figure 13. EM_{Hα} estimated over the KCWI footprint. The 2σ localization regions of the FRB are shown by the solid black ellipse. Here, we are showing the EM_{Hα} map without applying any reddening correction and assuming that the gas temperature is 10^4 K throughout.

star observation). Given that the FRB is located at the edge of this emission, it is likely that the clump is much more compact; thus, the true H α flux is even lower at the FRB location, and commensurately, our DM_{host,ISM} estimate is lower too. This could imply a significant circumburst contribution to the FRB DM. Indeed, space-based imaging with JWST obtained by P. K. Blanchard et al. (2025) revealed that the FRB localization region is consistent with a faint pointlike source ($\gtrsim 30 \text{ mag}$ in F150W2), and the higher-resolution data confirm that the 1σ localizations are well outside the nearby star-forming clump. This observation could even imply a negligible DM_{host,ISM} with all of the remaining DM in the budget arising from the circumburst medium.

6. Discussion

6.1. Repetition

No repeat bursts from FRB 20250316A have been detected in 269.77 hr of CHIME/FRB’s exposure toward its sky position, and the morphology of the original detection

(broadband emission spanning the entire observable 400 MHz and only $\lesssim 1 \text{ ms}$ in intrinsic duration; see Figure 4) is similar to that of other one-off events.

Our implied 99.7% upper-limit rate ($0.015 \text{ bursts hr}^{-1}$ above 15 Jy ms; Section 4.4) is not in tension with the repeater rates seen from CHIME/FRB’s sample. The measured burst rates in CHIME/FRB Collaboration et al. (2023) span 0.001–3 bursts hr^{-1} above 5 Jy ms for established repeaters. To compare the rate upper limits derived from this work more directly, we can recalculate this rate using the same assumptions as used by CHIME/FRB Collaboration et al. (2023): assuming burst arrival times are Poisson and scaling the upper limit on the rate we derive to 5 Jy ms assuming a power-law index of -1.5 . Based on these assumptions, and combining the CHIME/FRB data and the HyperFlash *L*-band data, we place a 99.7% Poisson upper limit on the repetition rate of $\sim 0.001 \text{ bursts hr}^{-1}$ above 5 Jy ms. Considering only the HyperFlash *L*-band data, scaled with the assumptions above, we derive a 99.7% upper limit on the repetition rate of $0.1 \text{ bursts hr}^{-1}$ above 5 Jy ms.

In addition to being highly clustered in time, evidence of months- to years-long repeater “lifetimes” has begun to emerge; for example, FRB 20201124A, FRB 20220912A, and FRB 20240209A were not detected for years by CHIME/FRB until their initial discovery, at which point they were in hyperactive phases (A. E. Lanman et al. 2022; V. Shah et al. 2025; T. C. Abbott et al. 2025, in preparation). The former two sources were not detected by CHIME/FRB for years after their initial months-long hyperactive phases. The third known repeater, FRB 20180916B, was discovered by CHIME and later was found to be emitting only in approximately 4 day windows every 16.3 days (CHIME/FRB Collaboration et al. 2020a), the first periodic behavior confirmed from an FRB source. For these reasons, the detection of only one burst by CHIME/FRB from FRB 20250316A is insufficient evidence that it is nonrepeating.

The implied upper-limit burst rate at low spectral energies relative to the implied burst rate at high spectral energies for FRB 20250316A, is, however, in significant tension with the known population of repeaters. The proximity of FRB 20250316A means that CHIME/FRB would likely have been sensitive to bursts about 1000 times less energetic than FRB 20250316A. Well-studied repeaters have burst spectral

energy distributions with steep power-law burst cumulative rates with indices ranging from -1.9 to -1.6 (Y.-K. Zhang et al. 2023; F. Kirsten et al. 2024; D. C. Konijn et al. 2024; O. S. Ould-Boukattine et al. 2024; J. Tian et al. 2025) at spectral energies comparable to FRB 20250316A and below. The steep -1.9 to -1.6 power-law rate distributions suggest that we would expect to detect these less energetic bursts $>10^5$ more frequently than bursts with the spectral energy of FRB 20250316A. We find the nondetection of bursts from FRB 20250316A with lower spectral energies incompatible with the properties of known repeaters at a minimum level of 3.7σ . Flatter spectral indices are required to relieve this tension: we find that only $\alpha > -0.6$ is consistent at the 3σ level. Shallow spectral indices have been measured for the higher-energy part of the broken power laws of FRB 20201124A and FRB 20220912A, but the spectral energy corresponding to the transition point between steep and shallow spectral indices for FRB 20250316A would need to be approximately 4 orders of magnitude lower than observed for these sources to be consistent (F. Kirsten et al. 2024; O. S. Ould-Boukattine et al. 2024). The FAST observations (H. Qian et al. 2025), which are sensitive to bursts 100 times less energetic than those detectable by CHIME/FRB, demonstrate that FRB 20250316A is not highly active just below the sensitivity limit of CHIME/FRB.

FRB 20250316A is in tension with the properties of all well-studied repeaters to date. We do not detect FRBs often within the volume of FRB 20250316A, and FRB 20250316A is the highest-S/N event among the FRBs for which CHIME/FRB captured raw voltage data between the years 2019 and 2023.⁵⁷ The position of FRB 20250316A transits through our main lobe $<10^\circ$ from the zenith of CHIME/FRB and centrally through a corresponding row of east–west synthesized beams, which means CHIME/FRB would have been particularly sensitive to bursts from this location.

Higher-fluence events than FRB 20250316A are detected far into CHIME/FRB’s side lobes a few times per year (H.-H. Lin et al. 2024). Despite comparable fluences, the nondetection of lower-fluence bursts from main-lobe transits of FRB 20250316A’s position represent a substantially stronger constraint on the repetition than for main-lobe transits of the high-fluence side-lobe sources. This is because the rate of low-fluence bursts expected for the side-lobe detections is smaller on account of the much larger exposure time over which the high-fluence detection was made. In comparison, the rate of high-fluence bursts required to explain the detection of FRB 20250316A during its short main-lobe exposure implies a higher expected rate of low-fluence bursts. This difference in exposure leads to FRB 20250316A having a much greater inconsistency with the known repeater population than the sources with high-fluence side-lobe bursts.

6.2. Host Galaxy NGC 4141

The host galaxy NGC 4141 is a relatively nearby SBc galaxy with a distance of 37–44 Mpc, notable for its abundance of H II regions and for having hosted two recent Type II SNe, SN 2008X and SN 2009E (T. Boles 2008, 2009; D. Madison et al. 2008; A. Pastorello et al. 2012), and an unclassified optical transient, AT 2025erx (I. Andreoni &

A. Palmese 2025). While the CHIME/FRB Outrigger localization is not positionally coincident with either of these SNe and rules them out as related to the FRB, the occurrence of two SNe within a 15 yr span may point to an elevated SFR in the recent past (L.-G. Strolger et al. 2015; M. J. Michałowski et al. 2020) and demonstrates a global environment with active star formation. However, the ongoing SFR in the host is not elevated at $0.6 M_\odot \text{ yr}^{-1}$ (L. J. Kewley et al. 2005). Combined with its inferred stellar mass of $1.7 \times 10^9 M_\odot$ (D. O. Cook et al. 2023), the specific SFR is $\sim 3.5 \times 10^{-10} \text{ yr}^{-1}$, at the median value for the host galaxies of nonrepeating FRBs (A. C. Gordon et al. 2023). Moreover, the projected physical offset of the FRB of ~ 4.5 kpc from its host galaxy is also an average value compared to the population of FRBs (A. C. Gordon et al. 2025). Overall, NGC 4141 lies on the “star-forming main sequence” of galaxies at comparable redshifts (K. E. Whitaker et al. 2012) and is unremarkable given the typical ranges of such properties observed for FRB host galaxies (A. C. Gordon et al. 2023; K. Sharma et al. 2024).

6.3. Environment

Our results paint a picture of an FRB on the outskirts of a star-forming environment of slightly subsolar metallicity. The DM budget allows for $\sim 40 \text{ pc cm}^{-3}$ to be contributed locally from the ISM and circumburst material. This local DM is small compared to the estimated hundreds of pc cm^{-3} local contributions of FRB 20121102A and FRB 20190520B (S. P. Tendulkar et al. 2017; S. K. Ocker et al. 2022). FRB 20121102A and FRB 20190520B additionally show evidence of having extreme magnetoionic environments (A. Bodaghee et al. 2012; D. Michilli et al. 2018; R. Anna-Thomas et al. 2023) characterized by large excess RMs, whereas FRB 20250316A’s measured local $|\text{RM}| \lesssim 10 \text{ rad m}^{-2}$ is consistent with zero given the level of uncertainty on the foreground Galactic contribution to the RM.

Our scintillation results (Section 4.3) and H α measurements (Section 5.4.5) are both consistent with a relatively dense⁵⁸ ($\text{EM}/\text{DM}_{\text{host,ISM}} \gg 0.1 \text{ cm}^{-3}$; see B. M. Gaensler et al. 2008) ionized cloud or screen that is $\lesssim 60$ pc in front of the FRB, over and above any intervening diffuse ionized gas in NGC 4141. While we cannot rule out such a discrete source at our limited spatial resolution, these properties are consistent with the FRB being inside or immediately behind the outskirts of the adjacent star-forming region, whose center is separated in projection from the FRB by 190 ± 20 pc. We therefore propose that the FRB is physically associated with this region and that the true offset of the FRB from the region’s center is not too different from its projected offset. The observed 190 ± 20 pc offset between this star-forming region is similar to the case for FRB 20180916B, which is offset by 250 pc from the center of a star-forming complex. If we follow the logic from S. P. Tendulkar et al. (2021) for FRB 20180916B, assuming that FRB 20250316A’s progenitor was formed near the center of the star formation region, we can estimate the minimum age of the FRB source given the observed offset and likely kick velocities by progenitors of interest. This is particularly constraining for the young magnetar scenario of FRBs, in which, if one assumes typical velocities from

⁵⁷ We search this sample because the real-time detection S/N is not an accurate predictor of the true S/N; see Section 2.1.

⁵⁸ When inferring $\text{DM}_{\text{host,ISM}}$ from the DM budgeting arguments and accounting for uncertainty

magnetars and pulsars in our own Galaxy (between 60 and 750 km s⁻¹ for 90% of observed pulsars, magnetars, and neutron stars in binaries; G. Hobbs et al. 2005; H. Ding et al. 2020), implies ages of 2×10^5 – 3×10^6 yr for the source, much longer than the typical active lifetimes of magnetars in our own Galaxy (S. A. Olausen & V. M. Kaspi 2014; V. M. Kaspi & A. M. Beloborodov 2017). However, using the fit from P. Disberg & I. Mandel (2025) of the distribution of kick velocities for <10 Myr isolated neutron stars, which spans a wider range of velocities than those considered in S. P. Tendulkar et al. (2021), and accounting for uncertainties in the measured offset and best-fit parameters, we estimate a 5% probability of observing such an offset for source ages less than 10 kyr. Even this slight tension between the offsets of FRB 20250316A and FRB 20180916B and the age of young magnetars can be relieved if one assumes that the neutron star/magnetar is created in situ via a runaway OB star.

Importantly, however, from JWST near-infrared imaging, P. K. Blanchard et al. (2025) find stars with a similar population age to those in the star formation region colocated with the FRB localization, indicative that the stellar population associated with the H II region extends beyond its apparent size in the KCWI images. Therefore, the authors conclude that a neutron star could have formed in situ, and as a result, one cannot place a meaningful constraint on its age based on the observed offset from the center of the star-forming region.

Other similarities between FRB 20250316A and FRB 20180916B are their expected DM_{host} contributions (40 and 70 pc cm⁻³, respectively; B. Marcote et al. 2020) and that both lack compact persistent radio counterparts. Of course, FRB 20250316A does not seem to be a repeater, whereas FRB 20180916B exhibits a ~ 16.3 day periodic activity cycle. The local environment of FRB 20180916B has an estimated metallicity of $12 + \log(\text{O}/\text{H}) = 8.4$, or $\log(Z/Z_{\odot}) \sim -0.3$, which is consistent with the metallicity of its host, as well as with NGC 4141, the host of FRB 20250316A ($12 + \log(\text{O}/\text{H}) \sim 8.2$; F. Taddia et al. 2013). We estimate a slightly higher gas-phase metallicity of ~ 8.6 or $\log(Z/Z_{\odot}) \sim -0.1$ for the local environment of FRB 20250316A (Section 5.4.3) compared to the average value for NGC 4141 and substantially higher than the mean values at deprojected normalized distances similar to the measured offset of FRB 20250316A, $\log(Z/Z_{\odot}) \approx -0.4$ (F. Taddia et al. 2013).

The local metallicity of the FRB environment is consistent with the distribution of global metallicity measurements of K. Sharma et al. (2024), who interpret the observed preferential occurrence of FRBs in high-mass galaxies as a preference for high-metallicity environments and hence favor progenitors like CCSNe of stellar merger remnants. This disfavors transient progenitors, which are in preferentially low-metallicity environments including superluminous SNe (T.-W. Chen et al. 2017) and long gamma-ray bursts (P. K. Blanchard et al. 2024). Our VLBI observations (Section 3.1.2) also rule out afterglow emission like that associated with a long gamma-ray burst that went off within the last ~ 10 yr⁵⁹ (L. Rhodes et al. 2020). Short GRB radio afterglows have been detected up to ~ 30 days postburst

(G. Schroeder et al. 2024) with $L_{\nu} \gtrsim 10^{39}$ erg s⁻¹ Hz⁻¹ at roughly GHz frequencies (W. Fong et al. 2015), which is 1000 times brighter than what our EVN limits would have been sensitive to 9 days after FRB 20250316A.

In fact, the proximity of FRB 20250316A allows us to place the deepest specific luminosity limit on any associated PRS with a nonrepeater to date, with $L_{\nu} < 4.2 \times 10^{25}$ erg s⁻¹ Hz⁻¹ at 4.9 GHz and $L_{\nu} < 2.2 \times 10^{25}$ erg s⁻¹ Hz⁻¹ at 9.9 GHz. Prior to FRB 20250316A, the deepest limit on a nonrepeater was set by FRB 20220319D with an upper limit of 1.8×10^{26} erg s⁻¹ Hz⁻¹ (C. J. Law et al. 2024). The limits imposed by our observations point to a radio environment more in line with that of FRB 20200120E, with the repeater localized to a globular cluster in M81, with a limit on a radio counterpart of $L_{\nu} \leq 3.1 \times 10^{23}$ erg s⁻¹ Hz⁻¹ at 1.5 GHz (F. Kirsten et al. 2022). Much like FRB 20200120E, FRB 20250316A stands in contrast to the specific luminosities of the known sample of PRSs associated with some repeating FRBs, interpreted as dense magnetospheric nebular environments with specific luminosities ranging from 10^{27} to 10^{29} erg s⁻¹ Hz⁻¹ (B. Marcote et al. 2017; C. H. Niu et al. 2022; S. Bhandari et al. 2023; G. Bruni et al. 2024, 2025b). Additionally, we can rule out a pulsar-wind-like nebula that is $\gtrsim 20\times$ more luminous than the Crab, with a present-day specific luminosity of $\sim 2 \times 10^{24}$ erg s⁻¹ Hz⁻¹ at 4.93 GHz (V. Trimble 1968; R. A. Perley & B. J. Butler 2017). Our observations cannot rule out emission like that of the SN remnant surrounding SGR 1935+2154, which is about 1000 times less luminous than our specific luminosity upper limits (R. Kothes et al. 2018).

Given FRB 20250316A's apparent tension with the spectral energy distributions of the repeating population and nearby nature of the burst, it is interesting to consider the gravitational-wave (GW) counterpart that would be expected along with a cataclysmic merger scenario. Two sites, Hanford and Livingston, of the Laser Interferometer Gravitational-Wave Observatory were operating in the 5 hr before and 2 hr after the arrival of FRB 20250316A and had an average sensitivity at S/N = 8 to binary neutron star inspirals to distances out to about 150 Mpc, about 3 times more distant than FRB 20250316A,⁶⁰ but no alerts were issued. Generally, it is expected that in these near-simultaneous windows around a binary neutron star merger, the ejecta environment would be opaque to the radio emission corresponding to what is observed at 400–800 MHz for FRB 20250316A (M. Bhardwaj et al. 2024a), although there are some models that predict near-simultaneous counterparts (e.g., B. Zhang 2014). We cannot, however, rule out a GW counterpart that occurred decades or centuries before FRB 20250316A.

There is no significant X-ray emission detected and no evidence for X-ray variability from this source (see Section 3.3). The 0.5–10.0 keV, 99.7% upper limits on the unabsorbed flux are of order 10^{-13} erg cm⁻² s⁻¹, or 10^{40} erg s⁻¹ assuming a source distance of 40 Mpc, both limits assuming an isotropic emission with a $\Gamma = 2$ power-law spectrum, absorbed by an $N_{\text{H}} = 1.4 \times 10^{20}$ cm⁻² neutral hydrogen column. Higher absorptive columns, like those expected if the source was located in a decades-old SN remnant (B. D. Metzger et al. 2017), could decrease the constraining power of these X-ray upper limits considerably, but neither our historical SN data nor the JWST observations

⁵⁹ We infer that the luminosity limits from our VLBI observations would be sensitive at the 3σ level to a typical long GRB afterglow on a timescale of 10 yr assuming a power-law drop-off in luminosity and extrapolating to 1.3 GHz (J. Granot & R. Sari 2002).

⁶⁰ Sensitivity according to the detector status summary page, https://gwosc.org/detector_status/day/20250316/, accessed 2025 May 19.

(P. K. Blanchard et al. 2025) support the presence of a very young SN remnant. The persistent X-ray limits rule out most ultraluminous X-ray sources at the position of FRB 20250316A (M. C. i. Bernadich et al. 2022), in line with luminosities that have been previously ruled out for other FRBs (T. Eftekhari et al. 2023; A. B. Pearlman et al. 2025b). This persistent X-ray limit cannot, however, rule out the presence of a Crab-like SN remnant or pulsar wind nebula, which is about 1000 times less luminous than the X-ray limit (A. B. Pearlman et al. 2025b).

7. Conclusion

The VLBI localization capabilities of the newly operational CHIME Outrigger array have enabled ~ 50 – 100 mas localizations of FRBs detected by CHIME/FRB’s wide field of view. The continental baselines achieve a precision well matched to the highest-resolution instruments at other wavelengths (e.g., JWST; P. K. Blanchard et al. 2025), allowing for unambiguous host associations and opening the door to spatially resolved, multi-wavelength studies that will address key questions about the sources of FRBs and maximize the utility of FRBs as cosmological probes.

The full Outrigger array localization of FRB 20250316A, paired with its proximity, allowed for the 13 pc precision localization and deep multiwavelength environment study of a nonrepeating FRB. Rapid MMT and Gemini follow-up observations allowed us to rule out transient optical emission above $M_r \approx -8$ mag 9 days after the event. Regular-cadence Coddennham Observatory and KAIT observations disfavor luminous optical transients like CCSNe and Type Ia SNe, which could be consistent with the location of FRB 20250316A for nearly 25 yr before the radio burst. The spectral energy of FRB 20250316A, particularly given our sensitivity toward this line of sight, was found to be inconsistent at a $>3.7\sigma$ level with having arisen from the burst energy distributions of known repeaters. We expect this source to remain the observational limit of certainty that a source is a nonrepeater given the rarity of detections this high above CHIME/FRB’s fluence threshold. If there is a distinct population of nonrepeating FRBs, given this apparent tension with the known repeater population, our study of FRB 20250316A provides unique insight into the local environment of a source, most likely from that nonrepeating population.

KCWI data allowed us to probe the gas density, metallicity, nature of gas ionization, dust extinction, and SFR in the environment of the FRB via emission line fluxes and revealed that FRB 20250316A is offset by 190 ± 20 pc from the center of the most proximal star formation region. The observed scintillation and scattering timescales additionally place a scattering screen within about 60 pc in front of FRB 20250316A, and we propose that the scattering screen is likely physically associated with the $H\alpha$ /star-forming region seen by KCWI. In this case, the true offset of the FRB from the region’s center is similar to its projected offset.

By itself, the lack of strong apparent star formation at the location of FRB 20250316A, coupled with limits at the FRB position on stars with $M \gtrsim 20 M_\odot$ (P. K. Blanchard et al. 2025), could have been interpreted as being in tension with a young (10–100 Myr) compact object like a magnetar. However, P. K. Blanchard et al. (2025) show that the locations of young stars in the vicinity of FRB 20250316A indicate that the observations of FRB 20250316A are not inconsistent with a compact object formed in situ.

One can imagine needing to consider many possible conclusions about the source of FRB 20250316A if we only had access to a CHIME/FRB-core-level localization (\sim arcminutes) or even a localization using only the first CHIME/FRB Outrigger (\sim tens of arcseconds), especially given the recent SNe in NGC 4141. For example, the local metallicity has implications for comparisons to known transient populations. Yet the measured local gas-phase metallicity is higher than the average host value and even the metallicity extrapolated to the measured offset of the FRB position.

Instead, zooming into the ~ 13 pc environment tells a much richer story: we find a clean radio environment with a relatively small DM contribution for the host and local environment compared to other FRBs, a slightly subsolar gas-phase metallicity, and a 190 ± 20 pc offset of the source from the nearest knot of star formation. This highlights the constraining power that large numbers of subarcsecond-precision localized FRBs, particularly one-off FRBs, will represent in the future. The incoming wealth of precisely localized FRBs from the now-operational CHIME Outriggers (CHIME/FRB Collaboration et al. 2025a), and eventually also from planned telescopes like the Canadian Hydrogen Observatory and Radio-transient Detector and the Deep Synoptic Array, will be revolutionary for disentangling multiple populations of FRBs and unveiling their sources (G. Hallinan et al. 2019; J. Kocz et al. 2019; K. Vanderlinde et al. 2019).

Acknowledgments

We thank Lauren Rhodes for inspiring the RBFLOAT name and for helpful comments that increased the quality of the draft. We also thank Reshma Anna Thomas for inspecting burst candidates from *realfast*. We are deeply grateful to Keith Gendreau, Zaven Arzoumanian, and Elizabeth Ferrera for promptly scheduling the NICER observations and for their support of our work. This work benefited from early access to the scintillometry methods described in S. Pradeep E. T. et al. (2025), and we are grateful to Sachin Pradeep E. T. and coauthors for sharing it. We also thank Jillian Rastinejad, who kindly triggered the first epoch of the MMT observations under her ToO program. We also thank the statistics editor for providing valuable context on the limitations of Schmidt’s V/V_{\max} method.

B.C.A. is supported by a Fonds de Recherche du Québec—Nature et Technologies (FRQNT) Doctoral Research Award. M. B. is a McWilliams fellow and an International Astronomical Union Gruber fellow. M.B. also receives support from the McWilliams seed grants. A.M.C. is a Banting Postdoctoral Researcher. A.P.C. is a Vanier Canada Graduate Scholar. M.D. is supported by a CRC Chair, Natural Sciences and Engineering Research Council of Canada (NSERC) Discovery Grant, CIFAR, and by the FRQNT Centre de Recherche en Astrophysique du Québec (CRAQ). Y.D. is supported by the National Science Foundation Graduate Research Fellowship under grant No. DGE-2234667. G.M.E. acknowledges funding from NSERC through Discovery Grant RGPIN-2020-04554. W.F. gratefully acknowledges support by the National Science Foundation (NSF) under grants AST-2206494 and AST-2308182 and CAREER grant AST-2047919, the David and Lucile Packard Foundation, the Alfred P. Sloan Foundation, and the Research Corporation for Science Advancement through Cottrell Scholar award #28284. E.F. and S.S.P. are supported by the National Science Foundation (NSF) under grant No. AST-2407399. J.W.T.H. and the AstroFlash research group acknowledge support from a Canada

Excellence Research Chair in Transient Astrophysics (CERC-2022-00009), an Advanced Grant from the European Research Council (ERC) under the European Union’s Horizon 2020 research and innovation program (“EuroFlash”; grant agreement #101098079), and an NWO-Vici grant (“AstroFlash”; VI.C.192.045). V.M.K. holds the Lorne Trottier Chair in Astrophysics & Cosmology, a Distinguished James McGill Professorship, and receives support from an NSERC Discovery Grant (RGPIN 228738-13). C.L. acknowledges support from the Miller Institute for Basic Research in Science at UC Berkeley. K.W.M. holds the Adam J. Burgasser Chair in Astrophysics and received support from NSF grant AST-2018490. K.T.M. is supported by an FRQNT Master’s Research Scholarship. J.M.P. acknowledges the support of an NSERC Discovery Grant (RGPIN-2023-05373). D.M. acknowledges support from the French government under the France 2030 investment plan as part of the Initiative d’Excellence d’Aix-Marseille Université—A*MIDEX (AMX-23-CEI-088). M.N. is a Fonds de Recherche du Québec—Nature et Technologies (FRQNT) postdoctoral fellow. K.N. is an MIT Kavli Fellow. A.P. is funded by the NSERC Canada Graduate Scholarships—Doctoral program. A.B.P. is a Banting Fellow, a McGill Space Institute (MSI) Fellow, and a FRQNT postdoctoral fellow. U.P. is supported by NSERC (funding reference number RGPIN-2019-06770, ALLRP 586559-23), Canadian Institute for Advanced Research (CIFAR), AMD AI Quantum Astro. Z.P. is supported by an NWO Veni fellowship (VI.Veni.222.295). M.W. S. acknowledges support from the Trottier Space Institute Fellowship program. K.R.S. is supported by a Fonds de Recherche du Québec—Nature et Technologies (FRQNT) Doctoral Research Award. S.M.R. is a CIFAR Fellow and is supported by the NSF Physics Frontiers Center award 2020265. P.S. acknowledges the support of an NSERC Discovery Grant (RGPIN-2024-06266). V.S. is supported by a Fonds de Recherche du Québec—Nature et Technologies (FRQNT) Doctoral Research Award. K.S. is supported by the NSF Graduate Research Fellowship Program. S.S. is supported by the joint Northwestern University and University of Chicago Brinson Fellowship. C.D.K. gratefully acknowledges support from the NSF through AST-2432037, the HST Guest Observer Program through HST-SNAP-17070 and HST-GO-17706, and JWST Archival Research through JWST-AR-6241 and JWST-AR-5441. I.H.S. is supported by an NSERC Discovery Grant and by the Canadian Institute for Advanced Research. D.C.S. is supported by an NSERC Discovery Grant (RGPIN-2021-03985) and by a Canadian Statistical Sciences Institute (CANSSI) Collaborative Research Team Grant. F.K. acknowledges support from Onsala Space Observatory for the provisioning of its facilities/observational support. The Onsala Space Observatory national research infrastructure is funded through Swedish Research Council grant 2017-00648. A.V.F. and W.Z. are grateful for financial support from the Christopher R. Redlich Fund, Gary and Cynthia Bengier, Clark and Sharon Winslow, and Alan Eustace and Kathy Kwan (W.Z. is a Bengier–Winslow–Eustace Specialist in Astronomy).

We acknowledge that CHIME and the k’ni?atn k’l’stk’masqt Outrigger (KKO) are built on the traditional, ancestral, and unceded territory of the Syilx Okanagan people. K’ni?atn k’l’stk’masqt is situated on land leased from the Imperial Metals Corporation. We are grateful to the staff of the Dominion Radio Astrophysical Observatory, which is operated by the National Research Council of Canada. CHIME operations are funded by a grant from the NSERC Alliance

Program and by support from McGill University, University of British Columbia, and the University of Toronto. CHIME/FRB Outriggers are funded by a grant from the Gordon & Betty Moore Foundation. We are grateful to Robert Kirshner for early support and encouragement of the CHIME/FRB Outriggers Project and to Dušan Pejaković of the Moore Foundation for continued support. CHIME was funded by a grant from the Canada Foundation for Innovation (CFI) 2012 Leading Edge Fund (Project 31170) and by contributions from the provinces of British Columbia, Québec, and Ontario. The CHIME/FRB Project was funded by a grant from the CFI 2015 Innovation Fund (Project 33213), contributions from the provinces of British Columbia and Québec, and the Dunlap Institute for Astronomy and Astrophysics at the University of Toronto. Additional support was provided by CIFAR, the Trottier Space Institute at McGill University, and the University of British Columbia. The CHIME/FRB baseband recording system is funded in part by a CFI John R. Evans Leaders Fund award to I.H.S. The National Radio Astronomy Observatory is a facility of the NSF operated under cooperative agreement by Associated Universities, Inc. The Fast and Fortunate for FRB Follow-up team acknowledges support from NSF grants AST-1911140, AST-1910471, and AST-2206490. FRB research at WVU is supported by NSF grants AST-2006548 and AST-2018490.

MMT Observatory access was supported by Northwestern University and the Center for Interdisciplinary Exploration and Research in Astrophysics (CIERA). Observations reported here were obtained at the MMT Observatory, a joint facility of the University of Arizona and the Smithsonian Institution. Some of the data presented herein were obtained at the W. M. Keck Observatory, which is operated as a scientific partnership among the California Institute of Technology, the University of California, and the NASA. The Observatory was made possible by the generous financial support of the W. M. Keck Foundation. The authors wish to recognize and acknowledge the very significant cultural role and reverence that the summit of Maunakea has always had within the indigenous Hawaiian community. We are most fortunate to have the opportunity to conduct observations from this mountain.

This work is based in part on observations carried out using the 32 m radio telescope operated by the Institute of Astronomy of the Nicolaus Copernicus University in Toruń (Poland) and supported by a Polish Ministry of Science and Higher Education SpUB grant. This work makes use of data from the Westerbork Synthesis Radio Telescope owned by ASTRON. ASTRON, the Netherlands Institute for Radio Astronomy, is an institute of the Dutch Scientific Research Council NWO (Nederlandse Organisatie voor Wetenschappelijk Onderzoek). We thank the Westerbork operators Richard Blaauw, Jurjen Sluman, and Henk Mulder for scheduling and supporting observations. The Nançay Radio Observatory is operated by the Paris Observatory, associated with the French Centre National de la Recherche Scientifique (CNRS), and partially supported by the Region Centre in France. We acknowledge financial support from “Programme National de Cosmologie et Galaxies” (PNCG) and “Programme National Hautes Energies” (PNHE) funded by CNRS/INSU-IN2P3-INP, CEA and CNES, France.

KAIT and its ongoing operation were made possible by donations from Sun Microsystems, Inc., the Hewlett-Packard Company, AutoScope Corporation, Lick Observatory, the

NSF, the University of California, the Sylvia & Jim Katzman Foundation, and the TABASGO Foundation. Research at Lick Observatory is partially supported by a generous gift from Google, Inc.

The European VLBI Network is a joint facility of independent European, African, Asian, and North American radio astronomy institutes. Scientific results from data presented in this publication are derived from the following EVN project code: EN006 & EL071.

The National Radio Astronomy Observatory is a facility of the National Science Foundation operated under cooperative agreement by Associated Universities, Inc. This work made use of the Swinburne University of Technology software correlator, developed as part of the Australian Major National Research Facilities Programme and operated under licence. The NICER mission and portions of the NICER science team activities are funded by the National Aeronautics and Space Administration (NASA).

We thank the staff of the GMRT that made these observations possible. GMRT is run by the National Centre for Radio Astrophysics of the Tata Institute of Fundamental Research.

Facilities: CHIME(FRB), EVN, GMRT, KAIT, MMT, NRT, Swift(XRT), VLA, VLBA, WSRT.

Software: photutils (L. Bradley et al. 2024).

Appendix A CHIME/FRB’s Sensitivity and Exposure toward FRB 20250316A

The position of FRB 20250316A transits through all four east–west formed beams in its corresponding beam row at near-peak sensitivity. We define its exposure as the total

amount of time that the position of FRB 20250316A was within the FWHM of a CHIME-formed beam evaluated at 600 MHz (the center of the observing band) and both the telescope and real-time pipeline were operational and performing at an acceptable level of sensitivity. Our regular procedure for estimating our sensitivity or fluence threshold for a given source leverages the detection S/N, detection S/N threshold, estimated fluence of a burst from that source, and a primary beam correction. The primary beam correction is dependent on the position of the source, and thus the sensitivity is averaged over the localization uncertainty region of the source weighted by the probability density of each position. This is necessary because the system response can vary significantly over the nonnegligible positional uncertainty for bursts where CHIME/FRB captured total intensity only.

For FRB 20250316A, there is negligible positional uncertainty, owing to the VLBI localization, but we do not know the true detection S/N given the significant masking of this bright burst (as discussed above). Thus, instead of the regular procedure, we estimate the fluence threshold to be 0.5 Jy ms, which corresponds to the fifth percentile of the 68% upper-limit values of fluence thresholds from CHIME/FRB’s Second Catalog of FRBs detected at zenith angles within 1° of FRB 20250316A (CHIME/FRB Collaboration et al. 2025b). We excluded sensitivity thresholds from repeat bursts from this distribution as they have a lower S/N callback threshold in the real-time pipeline. We motivate the choice of the fifth percentile given the negligible positional uncertainty of FRB 20250316A and its central transit through a formed beam row. CHIME/FRB’s daily exposure to FRB 20250316A in the two months following its detection are shown in Figure 14.

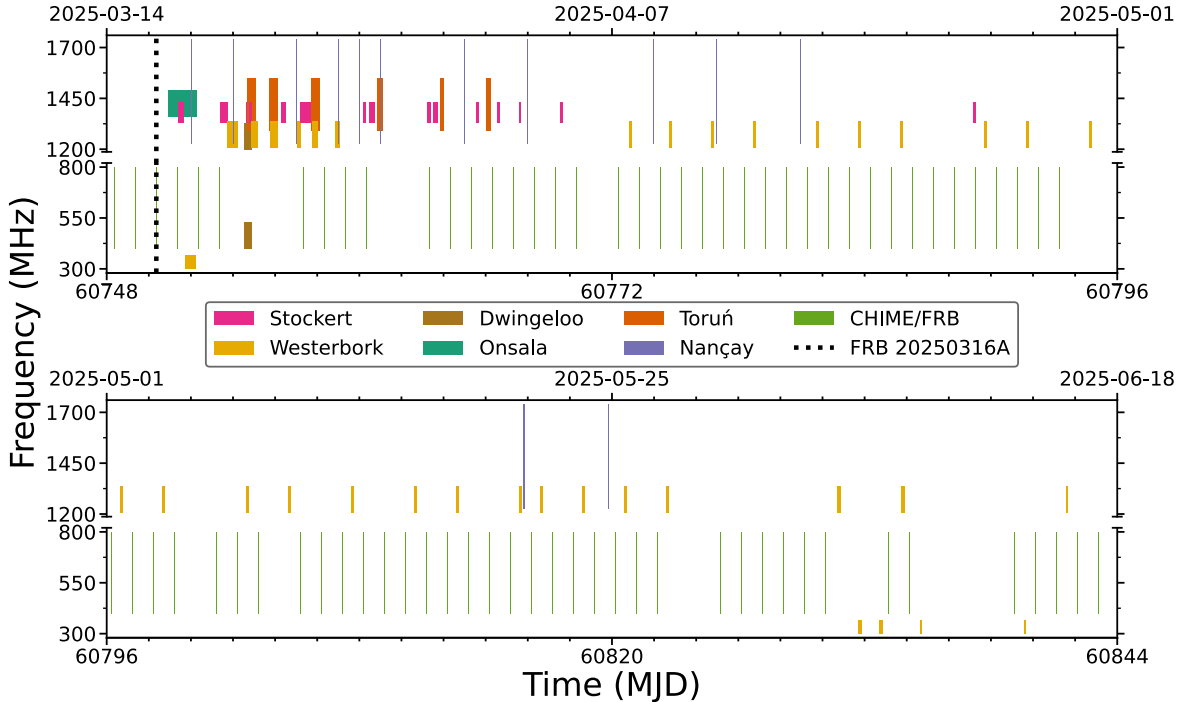


Figure 14. Overview of the FRB 20250316A observing campaign for repeat bursts by HyperFlash, ÉCLAT, and CHIME/FRB for 2 months following the discovery of the as-yet-nonrepeating burst. FRB 20250316A’s time of arrival is denoted with a dotted black vertical line. Each colored block represents an observation with a telescope at a given frequency (y-axis). Prior to the period shown above, CHIME/FRB additionally observed the position of FRB 20250316A nearly each sidereal day for ~ 11 minutes per transit since it commenced operations in 2018.

Appendix B

Continuum Radio Calibration and Images

For both EVN and HSA data, we performed phase-referenced observations, interleaving observations of FRB 20250316A and NVSS J121710+583526 (angular separation of 1°) on 5 minute intervals: 3.5 minutes on target and 1.5 minutes on the phase calibrator. Every four cycles, we interleaved observations of a check source, NVSS J120303+603119 for HSA and IVS B1212+602 for EVN. For the HSA observations, an intermediate scan was inserted every ~ 20 minutes to phase up the VLA (i.e., aligning the phases of the individual VLA dishes). We observed both NVSS J092703+390220 and NVSS J180045+782804 to serve as fringe finders. The visibilities for both EVN and HSA were reduced using standard procedures in the Astronomical Image Processing System (E. W. Greisen 2003). A priori system temperature and gain corrections were applied, followed by deriving instrumental delay corrections using a 1.5 minute interval on NVSS J092703+390220. The visibilities were manually inspected for RFI and/or periods when an antenna was not on source and subsequently flagged. Ionospheric corrections using the `vlbatecr` function were applied to the visibilities. Multiband delay solutions were derived using the phase

calibrator on 20 s intervals with either Effelsberg (EVN observations) or the VLA (HSA observations) as the reference antenna. Bandpass solutions were derived using NVSS J092703+390220. Once calibrated, the visibilities of the phase calibrator were exported for image processing using DIFMAP (M. C. Shepherd et al. 1994). Calibration solutions were improved via self-calibration of the phase calibrator (both phase and amplitude) and the corrections applied to the target visibilities. We validated our calibration techniques by imaging the respective check sources prior to imaging FRB 20250316A. The final set of calibrated visibilities were exported to search for compact, persistent radio emission. Assuming natural weighting, the resulting EVN and HSA dirty images had an rms of $9.2 \mu\text{Jy beam}^{-1}$ and $4.4 \mu\text{Jy beam}^{-1}$, respectively, in line with the expected thermal noise sensitivity limit. We detect maximum peaks in the dirty images at the $\sim 4.5\sigma$ levels; however, we identify no evidence of fringing and thus deem it unlikely to be of astrophysical origin. We place a 5σ upper limit on any radio flux associated with compact radio emission of $\leq 22 \mu\text{Jy}$ and $\leq 46 \mu\text{Jy}$ with the HSA and EVN, respectively. Residual dirty images obtained with both VLBI arrays are provided in Figure 15. A subset of the radio images is provided in Figure 16. A summary table of all continuum radio observations is provided in Table 3.

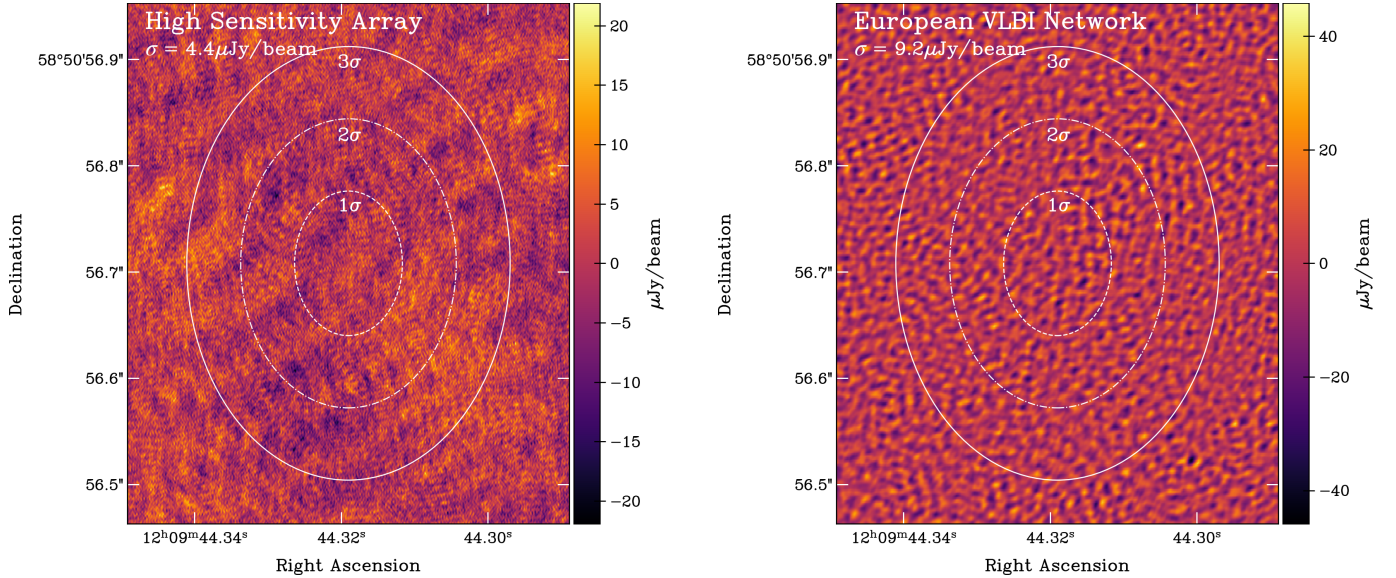


Figure 15. Residual dirty images of FRB 20250316A using the HSA (left) and EVN (right) at 4.9 GHz. The rms of each image is $\sigma = 4.4 \mu\text{Jy beam}^{-1}$ and $\sigma = 9.2 \mu\text{Jy beam}^{-1}$, respectively. Images are saturated to $\pm 5\sigma$. We overplot the 1σ , 2σ , and 3σ localization contours of the FRB as white ellipses, with the levels indicated on the image. We identify no evidence for compact radio emission in the field of FRB 20250316A, placing a 5σ upper limit on any PRS emission of $\leq 22 \mu\text{Jy}$.

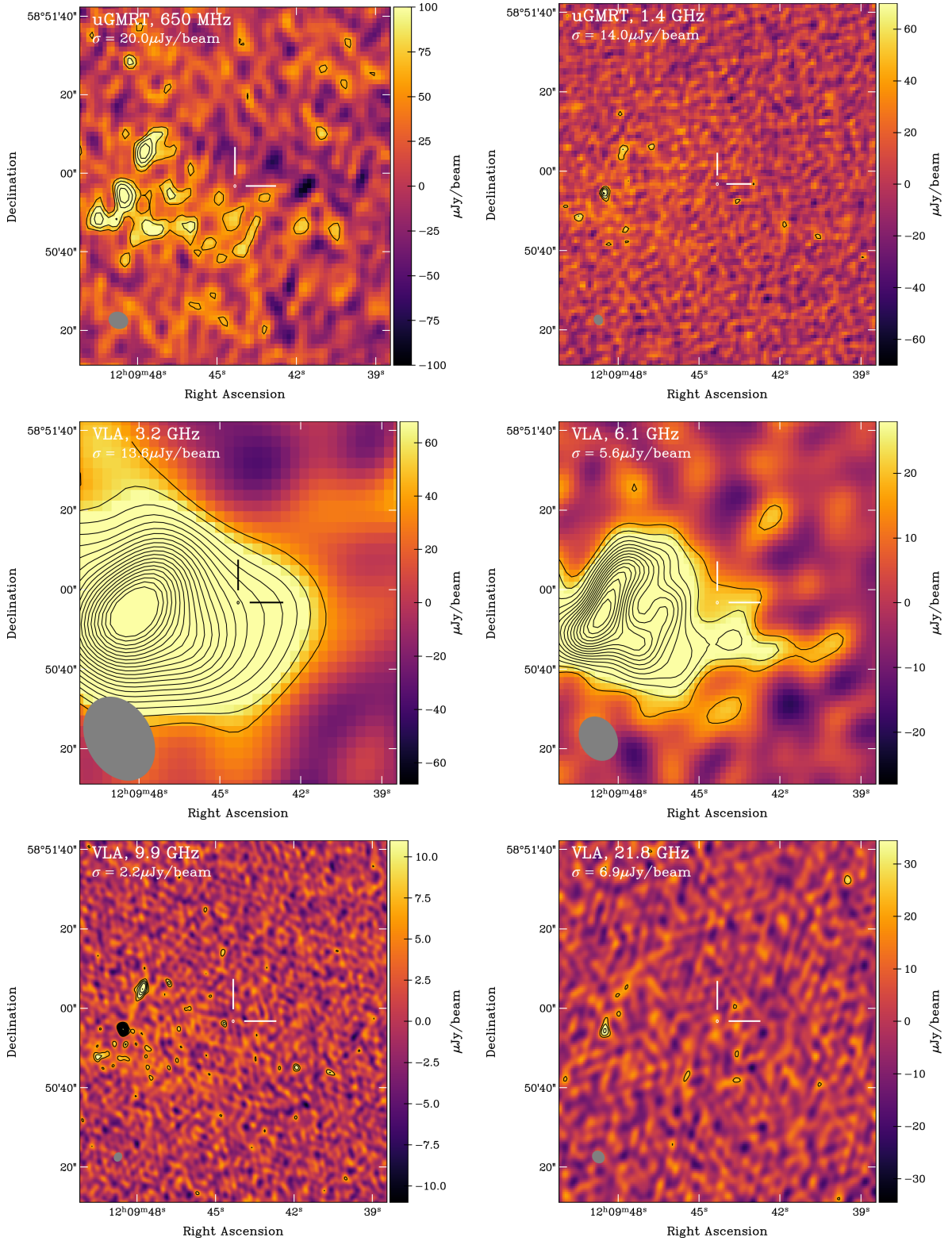


Figure 16. Multiband radio images of NGC 4141 using the VLA and the uGMRT. The FRB position is indicated by crosshairs, with the 5σ localization ellipse drawn at the center. Contours begin at 3σ and increase by factors of $\sqrt{2}$, where σ corresponds to the rms of the residuals. Images are saturated $\pm 5\sigma$. The synthesized beam is indicated in the bottom left of each image by a gray ellipse. Host galaxy emission dominates at low angular resolution and low frequencies, gradually fading as the angular resolution increases.

Table 3
Summary of Multiband, Multiepoch Continuum Radio Observations

Date (UTC)	Array ^a	ν^b (GHz)	σ^c ($\mu\text{Jy beam}^{-1}$)	$F_{\nu, \text{NGC 4141}}^d$ (mJy)	$L_{\nu, \text{PRS}}^e$ ($\text{erg s}^{-1} \text{Hz}^{-1}$)
2025 Mar 25	EVN	4.9	9.2	...	$< 8.8 \times 10^{25}$
2025 Mar 30	uGMRT	0.65	20	1.1 ± 0.1	$\leq 1.9 \times 10^{26}$
2025 Mar 31	uGMRT	1.4	14	2.3 ± 0.2	$\leq 1.3 \times 10^{26}$
2025 Apr 1	HSA	4.9	4.4	...	$\leq 4.2 \times 10^{25}$
2025 Apr 4	VLA	3.2	13.6	1.31 ± 0.07	$\leq 1.3 \times 10^{26}$
2025 Apr 4	VLA	6.1	5.6	0.72 ± 0.04	$\leq 5.4 \times 10^{25}$
2025 Apr 4	VLA	9.9	5.2	0.11 ± 0.01	$\leq 5.0 \times 10^{25}$
2025 Apr 4	VLA	21.8	6.9	< 0.035	$\leq 6.6 \times 10^{25}$
2025 May 10	VLA	3.2	13.5	1.31 ± 0.07	$\leq 1.3 \times 10^{26}$
2025 May 10	VLA	6.1	5.8	0.80 ± 0.04	$\leq 5.6 \times 10^{25}$
2025 May 10	VLA	9.9	5.6	0.13 ± 0.01	$\leq 5.4 \times 10^{25}$
2025 May 10	VLA	21.8	7.8	< 0.039	$\leq 7.5 \times 10^{25}$
2025 May 30	VLA ^f	9.9	2.2	0.11 ± 0.01	$\leq 2.1 \times 10^{25}$

Notes.

^a VLA = Very Large Array (D-configuration). HSA = High Sensitivity Array (VLBA + phased VLA). EVN = European VLBI Network. uGMRT = upgraded Giant Metrewave Radio Telescope.

^b Central observing frequency.

^c rms of residuals.

^d Integrated flux density associated with NGC 4141. Quoted values correspond to the flux density contained within 5σ contours. Uncertainties include both a statistical and a flat 5% systematic uncertainty, added in quadrature. If no flux above 5σ is detected, we quote the 5σ (statistical) upper limit.

^e Limits on any associated persistent radio counterpart. Upper limits on specific luminosity are quoted at the 5σ level assuming a luminosity distance of 40 Mpc.

^f VLA observations were performed in C-configuration.

Appendix C Radio Burst Morphology Modeling

We model the burst as two Gaussian components characterized by start times and widths (t_1, t_2, w_1, w_2), convolved with two thin screen scattering kernels characterized by scattering times referenced to 600 MHz and power-law scaling indices ($\tau_1, \tau_2, \alpha_1, \alpha_2$). We perform a joint maximum-likelihood fit of these parameters using the `Bilby` implementation of the `Dynesty` nested-sampling library to minimize the square of the residuals between our model and the observed dynamic spectra at 0.390625 MHz spectral resolution and $25.6 \mu\text{s}$ temporal resolution (G. Ashton et al. 2019; J. S. Speagle 2020). We assume prior independence among the model parameters and specify the joint prior distribution as the product of the following univariate distributions:

$$\begin{aligned} \log_{10}(\tau_1/[\text{s}]) &\sim \mathcal{U}[10^{-5}, 2 \times 10^{-4}], \\ \log_{10}(w_1/[\text{s}]) &\sim \mathcal{U}[10^{-5}, 5 \times 10^{-5}], \\ \tau_2 &\sim \mathcal{U}[2.1 \times 10^{-4}, 5 \times 10^{-3}] \text{s}, \end{aligned}$$

$$\begin{aligned} \log_{10}(w_2/[\text{s}]) &\sim \mathcal{U}[10^{-4}, 3 \times 10^{-4}], \\ \alpha_1 &\sim \mathcal{U}[-6, -2], \quad t_1 \sim \mathcal{U}[1.3, 2.0] \text{ms}, \\ \alpha_2 &\sim \mathcal{U}[-6, -2], \quad t_2 \sim \mathcal{U}[2.2, 3.0] \text{ms}, \\ \log_{10}(\sigma) &\sim \mathcal{U}[5, 50], \end{aligned}$$

where $\mathcal{U}[a, b]$ represents the uniform distribution on a closed interval $[a, b]$.

To account for the instrumental spectral ripple and any underlying spectral index of the intrinsic components, we normalize our model to the burst's time-integrated spectra and thereby fit only for the temporal shape of the burst as a function of frequency and time. Figure 17 shows the corner plot for our best-fit solution with the associated model and residuals compared against the data shown in Figure 18. We do not attempt to evaluate our goodness of fit using a χ^2 as the noise over the burst duration is dominated by physical source noise (the random fluctuations in the intrinsic signal; see J. S. Morgan & R. Ekers 2021 for an in-depth discussion) that is not captured by our smooth model.

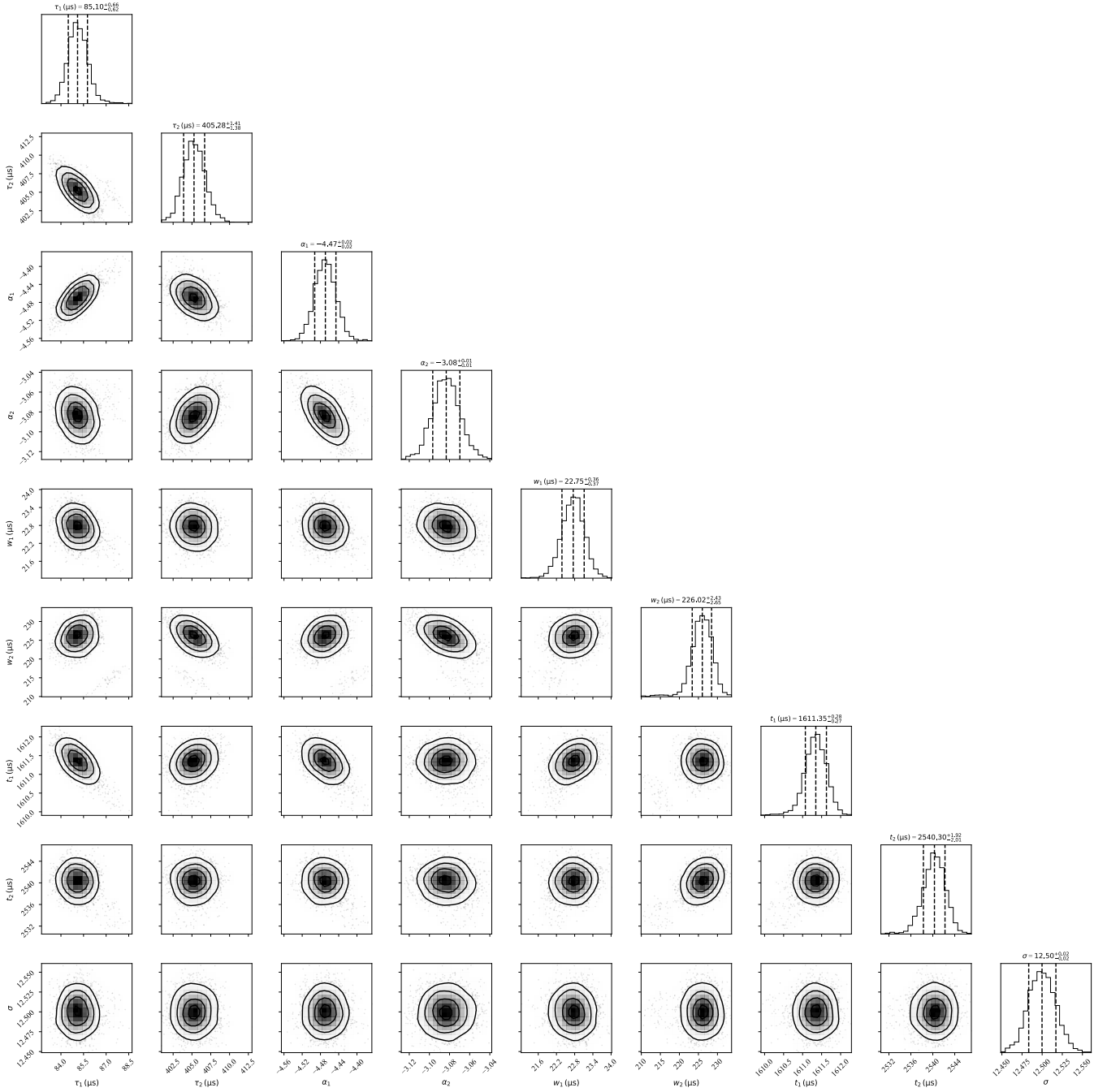


Figure 17. Best-fit solutions and marginalized errors for the two-screen, two-component model described in the text. Gaussianity in each parameter is consistent with a converged solution with some covariance between parameters indicating that our model is mildly degenerate but mutually constrained.

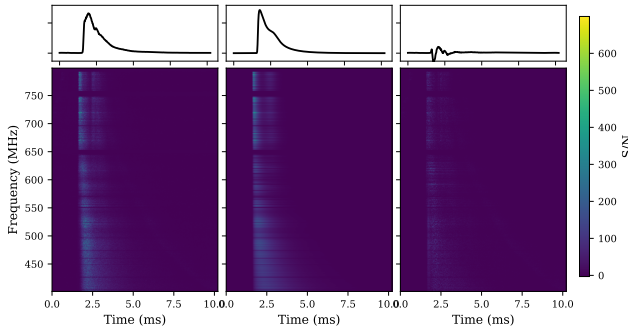


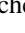




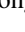













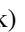
















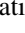









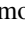






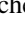




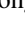











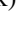



Figure 18. Comparison of the observed dynamic spectra of FRB 20250316A (left) with the best-fit model (middle) and squared residuals (right).

ORCID iDs

Thomas C. Abbott <https://orcid.org/0000-0001-5002-0868>
 Daniel Amouyal <https://orcid.org/0009-0005-5370-7653>
 Bridget C. Andersen <https://orcid.org/0000-0001-5908-3152>
 Shion E. Andrew <https://orcid.org/0000-0002-3980-815X>
 Kevin Bandura <https://orcid.org/0000-0003-3772-2798>
 Mohit Bhardwaj <https://orcid.org/0000-0002-3615-3514>
 Kalyani Bhopi <https://orcid.org/0000-0002-9218-1624>
 Yash Bhusare <https://orcid.org/0000-0002-5342-163X>
 Charanjot Brar <https://orcid.org/0000-0002-1800-8233>
 Alice Cai <https://orcid.org/0009-0001-0983-623X>

- Tomas Cassanelli  <https://orcid.org/0000-0003-2047-5276>
 Shami Chatterjee  <https://orcid.org/0000-0002-2878-1502>
 Jean-François Cliche  <https://orcid.org/0000-0001-6509-8430>
 Amanda M. Cook  <https://orcid.org/0000-0001-6422-8125>
 Alice P. Curtin  <https://orcid.org/0000-0002-8376-1563>
 Evan Davies-Veile  <https://orcid.org/0009-0002-1944-6398>
 Matt Dobbs  <https://orcid.org/0000-0001-7166-6422>
 Fengqiu Adam Dong  <https://orcid.org/0000-0003-4098-5222>
 Yuxin Dong
 (董雨欣)  <https://orcid.org/0000-0002-9363-8606>
 Gwendolyn Eadie  <https://orcid.org/0000-0003-3734-8177>
 Tarraneh Eftekhari  <https://orcid.org/0000-0003-0307-9984>
 Wen-fai Fong  <https://orcid.org/0000-0002-7374-935X>
 Emmanuel Fonseca  <https://orcid.org/0000-0001-8384-5049>
 B. M. Gaensler  <https://orcid.org/0000-0002-3382-9558>
 Nina Gusinskaia  <https://orcid.org/0000-0001-6128-3735>
 Jason W. T. Hessels  <https://orcid.org/0000-0003-2317-1446>
 Danté M. Hewitt  <https://orcid.org/0000-0002-5794-2360>
 Jeff Huang  <https://orcid.org/0000-0002-8043-0048>
 Naman Jain  <https://orcid.org/0009-0009-0938-1595>
 Ronniy. C. Joseph  <https://orcid.org/0000-0003-3457-4670>
 Lordrick Kahinga  <https://orcid.org/0009-0007-5296-4046>
 Victoria M. Kaspi  <https://orcid.org/0000-0001-9345-0307>
 Afrasiyab (Afrokk) Khan  <https://orcid.org/0009-0004-4176-0062>
 Bikash Kharel  <https://orcid.org/0009-0008-6166-1095>
 Adam E. Lanman  <https://orcid.org/0000-0003-2116-3573>
 Magnus L'Argent  <https://orcid.org/0000-0001-5523-6051>
 Mattias Lazda  <https://orcid.org/0000-0002-5857-4264>
 Calvin Leung  <https://orcid.org/0000-0002-4209-7408>
 Robert Main  <https://orcid.org/0000-0002-7164-9507>
 Lluís Mas-Ribas  <https://orcid.org/0000-0003-4584-8841>
 Kiyoshi W. Masui  <https://orcid.org/0000-0002-4279-6946>
 Kyle McGregor  <https://orcid.org/0000-0003-2111-3437>
 Ryan Mckinven  <https://orcid.org/0000-0001-7348-6900>
 Juan Mena-Parra  <https://orcid.org/0000-0002-0772-9326>
 Daniele Michilli  <https://orcid.org/0000-0002-2551-7554>
 Nicole Mulyk  <https://orcid.org/0000-0001-7491-046X>
 Mason Ng  <https://orcid.org/0000-0002-0940-6563>
 Kenzie Nimmo  <https://orcid.org/0000-0003-0510-0740>
 Ayush Pandhi  <https://orcid.org/0000-0002-8897-1973>
 Swarali Shivraj Patil  <https://orcid.org/0009-0008-7264-1778>
 Aaron B. Pearlman  <https://orcid.org/0000-0002-8912-0732>
 Ue-Li Pen  <https://orcid.org/0000-0003-2155-9578>
 Ziggy Pleunis  <https://orcid.org/0000-0002-4795-697X>
 J. Xavier Prochaska  <https://orcid.org/0000-0002-7738-6875>
 Masoud Rafiei-Ravandi  <https://orcid.org/0000-0001-7694-6650>
 Scott M. Ransom  <https://orcid.org/0000-0001-5799-9714>
 Gurman Sachdeva  <https://orcid.org/0009-0005-6633-3945>
 Mawson W. Sammons  <https://orcid.org/0000-0002-4623-5329>
 Ketan R. Sand  <https://orcid.org/0000-0003-3154-3676>
 Paul Scholz  <https://orcid.org/0000-0002-7374-7119>
 Vishwangi Shah  <https://orcid.org/0000-0002-4823-1946>
 Kaitlyn Shin  <https://orcid.org/0000-0002-6823-2073>
 Seth R. Siegel  <https://orcid.org/0000-0003-2631-6217>
 Sunil Simha  <https://orcid.org/0000-0003-3801-1496>
 Kendrick Smith  <https://orcid.org/0000-0002-2088-3125>
 Ingrid Stairs  <https://orcid.org/0000-0001-9784-8670>
 David C. Stenning  <https://orcid.org/0000-0002-9761-4353>
 Haochen Wang  <https://orcid.org/0000-0002-1491-3738>
 Ismaël Cognard  <https://orcid.org/0000-0002-1775-9692>
 Tammo Jan Dijkema  <https://orcid.org/0000-0001-7551-4493>
 Alexei V. Filippenko  <https://orcid.org/0000-0003-3460-0103>
 Marcin P. Gawroński  <https://orcid.org/0000-0003-4056-4903>
 Wolfgang Herrmann  <https://orcid.org/0000-0001-5806-446X>
 Charles D. Kilpatrick  <https://orcid.org/0000-0002-5740-7747>
 Franz Kirsten  <https://orcid.org/0000-0001-6664-8668>
 Shawn Knabel  <https://orcid.org/0000-0001-5110-6241>
 Omar S. Ould-Boukattine  <https://orcid.org/0000-0001-9381-8466>
 Hadrien Pagnat  <https://orcid.org/0000-0002-2603-6031>
 Weronika Puchalska  <https://orcid.org/0000-0003-2422-6605>
 William Sheu  <https://orcid.org/0000-0003-1889-0227>
 Aswin Suresh  <https://orcid.org/0009-0005-8230-030X>
 Aaron Tohuvavohu  <https://orcid.org/0000-0002-2810-8764>
 Tommaso Treu  <https://orcid.org/0000-0002-8460-0390>
 WeiKang Zheng  <https://orcid.org/0000-0002-2636-6508>

References

- Abbott, T. C., Zwaniga, A. V., Brar, C., et al. 2025, *AJ*, 169, 39
 Aggarwal, K., Budavári, T., Deller, A. T., et al. 2021, *ApJ*, 911, 95
 Andreoni, I., & Palmese, A. 2025, *TNSTR*, 2025-1016, 1
 Andrew, S. & CHIME/FRB Collaboration 2025, *ATel*, 17114, 1
 Andrew, S., Leung, C., Li, A., et al. 2025, *ApJ*, 981, 39
 Anna-Thomas, R., Connor, L., Dai, S., et al. 2023, *Sci*, 380, 599
 Ashton, G., Hübner, M., Lasky, P. D., et al. 2019, *ApJS*, 241, 27
 Baldwin, J. A., Phillips, M. M., & Terlevich, R. 1981, *PASP*, 93, 5
 Bassa, C. G., Tendulkar, S. P., Adams, E. A. K., et al. 2017, *ApJL*, 843, L8
 Becker, A., 2015 HOTPANTS: High Order Transform of PSF AND Template Subtraction, Astrophysics Source Code Library, ascl:1504.004
 Bernadich, M. C. i., Schwope, A. D., Kovlakas, K., Zezas, A., & Traulsen, I. 2022, *A&A*, 659, A188
 Bernales-Cortés, L., Tejos, N., Prochaska, J. X., et al. 2025, *A&A*, 696, A81
 Bertin, E., & Arnouts, S. 1996, *A&AS*, 117, 393
 Bhandari, S., Heintz, K. E., Aggarwal, K., et al. 2022, *AJ*, 163, 69
 Bhardwaj, M., Gaensler, B. M., Kaspi, V. M., et al. 2021, *ApJL*, 910, L18
 Bhandari, S., Marcote, B., Sridhar, N., et al. 2023, *ApJL*, 958, L19
 Bhardwaj, M., Michilli, D., Kirichenko, A. Y., et al. 2024b, *ApJL*, 971, L51
 Bhardwaj, M., Palmese, A., Magaña Hernández, I., D'Emilio, V., & Morisaki, S. 2024a, *ApJ*, 977, 122
 Bhardwaj, M., Snelders, M. P., Hessels, J. W. T., et al. 2025, arXiv, 2506.11915
 Blanchard, P. K., Berger, E., Andrew, S. E., et al. 2025, *ApJL*, 989, L49
 Blanchard, P. K., Villar, V. A., Chornock, R., et al. 2024, *NatAs*, 8, 774
 Bodaghee, A., Tomsick, J. A., Rodriguez, J., & James, J. B. 2012, *ApJ*, 744, 108
 Bohlin, R. C., Deustua, S., Narayan, G., et al. 2025, *AJ*, 169, 40
 Boles, T. 2008, *CBET*, 1239, 1
 Boles, T. 2009, *CBET*, 1648, 1
 Bradley, L., Sipőcz, B., Robitaille, T., et al., 2024 astropy/photutils: 2.0.2, Zenodo, doi:10.5281/zenodo.13989456
 Brentjens, M. A., & de Bruyn, A. G. 2005, *A&A*, 441, 1217
 Bruni, G., Piro, L., Thakur, A. L., et al. 2025a, *ATel*, 17120, 1
 Bruni, G., Piro, L., Yang, Y.-P., et al. 2024, *Natur*, 8027, 1014
 Bruni, G., Piro, L., Yang, Y.-P., et al. 2025b, *A&A*, 695, L12
 Burn, B. J. 1966, *MNRAS*, 133, 67
 Chabrier, G. 2003, *PASP*, 115, 763

- Chen, T.-W., Smartt, S. J., Yates, R. M., et al. 2017, *MNRAS*, **470**, 3566
- CHIME Collaboration, Amiri, M., Bandura, K., et al. 2022, *ApJS*, **261**, 29
- CHIME/FRB Collaboration, Amiri, M., Andersen, B. C., et al. 2020a, *Natur*, **582**, 351
- CHIME/FRB Collaboration, Amiri, M., Andersen, B. C., et al. 2021, *ApJS*, **257**, 59
- CHIME/FRB Collaboration, Amiri, M., Andersen, B. C., et al. 2025a, arXiv:2504.05192
- CHIME/FRB Collaboration, Amiri, M., Bandura, K., et al. 2018, *ApJ*, **863**, 48
- CHIME/FRB Collaboration, Andersen, B. C., Bandura, K., et al. 2023, *ApJ*, **947**, 83
- CHIME/FRB Collaboration, Andersen, B. C., Bandura, K. M., et al. 2020b, *Natur*, **587**, 54
- CHIME/FRB Collaboration, Abbott, T. C., Andersen, B. C., Andrew, S., et al. 2025b, *ApJS*, submitted
- Choi, J., Dotter, A., Conroy, C., et al. 2016, *ApJ*, **823**, 102
- Condon, J. J. 1992, *ARA&A*, **30**, 575
- Connor, L., Athukoralalage, W., Bieryla, A., et al. 2025, *ATel*, **17091**, 1
- Conroy, C., Gunn, J. E., & White, M. 2009, *ApJ*, **699**, 486
- Cook, A. M., Bhardwaj, M., Gaensler, B. M., et al. 2023, *ApJ*, **946**, 58
- Cook, D. O., Mazzarella, J. M., Helou, G., et al. 2023, *ApJS*, **268**, 14
- Cordes, J. M., & Lazio, T. J. W. 2002, arXiv:astro-ph/0207156
- Cordes, J. M., & McLaughlin, M. A. 2003, *ApJ*, **596**, 1142
- Cordes, J. M., Wharton, R. S., Spitler, L. G., Chatterjee, S., & Wasserman, I. 2016, arXiv:1605.05890
- Curtin, A. P., Andrew, S., Simha, S., et al. 2025, arXiv, arXiv:2506.10961
- Curtin, A. P., Sand, K. R., Pleunis, Z., et al. 2024, arXiv, arXiv:2411.02870
- Deller, A. T., Tingay, S. J., Bailes, M., & West, C. 2007, *PASP*, **119**, 318
- Desvignes, G., Barott, W. C., Cognard, I., Lespagnol, P., & Theureau, G. 2011, in AIP Conf. Ser. 1357, Radio Pulsars: An Astrophysical Key to Unlock the Secrets of the Universe, ed. M. Burgay et al. (Melville, NY: AIP), 349
- Dey, A., Schlegel, D. J., Lang, D., et al. 2019, *AJ*, **157**, 168
- Ding, H., Deller, A. T., Lower, M. E., et al. 2020, *MNRAS*, **498**, 3736
- Disberg, P., & Mandel, I. 2025, arXiv, arXiv:2505.22102
- Dong, Y., & CHIME/FRB Collaboration 2025, *ATel*, **17112**, 1
- Dong, Y., Eftekhari, T., Fong, W.-f., et al. 2024, *ApJ*, **961**, 44
- Dong, Y., Kilpatrick, C. D., Fong, W., et al. 2025, arXiv:2506.06420
- Dumas, G., Schinnerer, E., Tabatabaei, F. S., et al. 2011, *AJ*, **141**, 41
- Dunn, O. J. 1961, *JASA*, **56**, 52
- Eftekhari, T., Dong, Y., Fong, W., et al. 2025, *ApJL*, **979**, L22
- Eftekhari, T., Fong, W., Gordon, A. C., et al. 2023, *ApJ*, **958**, 66
- Feigelson, E. D., & Babu, G. J. 2012, arXiv:1205.2064
- Filippenko, A. V., Li, W. D., Treffers, R. R., & Modjaz, M. 2001, in ASP Conf. Ser. 246, IAU Colloq. 183: Small Telescope Astronomy on Global Scales, ed. B. Paczynski, W.-P. Chen, & C. Lemme (San Francisco, CA: ASP), 121
- Flewellling, H. A., Magnier, E. A., Chambers, K. C., et al. 2020, *ApJS*, **251**, 7
- Fong, W., Berger, E., Margutti, R., & Zauderer, B. A. 2015, *ApJ*, **815**, 102
- Fonseca, E., Pleunis, Z., Breitman, D., et al. 2024, *ApJS*, **271**, 49
- Gaensler, B. M., Madsen, G. J., Chatterjee, S., & Mao, S. A. 2008, *PASA*, **25**, 184
- Gaia Collaboration, Brown, A. G. A., Vallenari, A., et al. 2021, *A&A*, **649**, A1
- Gaia Collaboration, Klioner, S. A., Lindgren, L., et al. 2022, *A&A*, **667**, A148
- Gaia Collaboration, Vallenari, A., Brown, A. G. A., et al. 2023, *A&A*, **674**, A1
- Gardenier, D. W., Connor, L., van Leeuwen, J., Oostrum, L. C., & Petroff, E. 2021, *A&A*, **647**, A30
- Golay, W. W., Berger, E., Kumar, H., & Hiramatsu, D. 2025, *ATel*, **17111**, 1
- Good, D. C., Chawla, P., Fonseca, E., et al. 2023, *ApJ*, **944**, 70
- Gordon, A. C., Fong, W.-f., Deller, A. T., et al. 2025, arXiv:2506.06453
- Gordon, A. C., Fong, W.-f., Kilpatrick, C. D., et al. 2023, *ApJ*, **954**, 80
- Gordon, K., 2024 dust extinction, Zenodo:10.5281/zenodo.11235336
- Gordon, K. D., Clayton, G. C., Decleir, M., et al. 2023, *ApJ*, **950**, 86
- Granot, J., & Sari, R. 2002, *ApJ*, **568**, 820
- Greiner, J., Michałowski, M. J., Klose, S., et al. 2016, *A&A*, **593**, A17
- Greisen, E. W. 2003, in Information Handling in Astronomy—Historical Vistas, ed. A. Heck (Dordrecht: Kluwer), 109
- Hallinan, G., Ravi, V., Weinreb, S., et al. 2019, *BAAS*, **51**, 255
- Hewitt, D. M., Bhandari, S., Marcote, B., et al. 2024b, *MNRAS*, **529**, 1814
- Hewitt, D. M., Bhardwaj, M., Gordon, A. C., et al. 2024a, *ApJL*, **977**, L4
- HI4PI Collaboration, Ben Bekhti, N., Flöer, L., et al. 2016, *A&A*, **594**, A116
- Ho, A. Y. Q., Perley, D. A., Gal-Yam, A., et al. 2023, *ApJ*, **949**, 120
- Hobbs, G., Lorimer, D. R., Lyne, A. G., & Kramer, M. 2005, *MNRAS*, **360**, 974
- Horowitz, A., & Margalit, B. 2025, arXiv, arXiv:2504.08038
- Huang, Y., Lee, K.-G., Libeskind, N. I., et al. 2025, *MNRAS*, **538**, 2785
- Hutschenreuter, S., Haverkorn, M., Frank, P., Raycheva, N. C., & Enßlin, T. A. 2024, *A&A*, **690**, A314
- Jacobson-Galán, W. V., Dessart, L., Davis, K. W., et al. 2025, arXiv:2505.04698
- James, C. W. 2023, *PASA*, **40**, e057
- Jing, W. C., Han, J. L., Wang, C., et al. 2025, arXiv:2506.14519
- Kale, R., & Ishwara-Chandra, C. H. 2020, *ExA*, **51**, 95
- Kaspi, V. M., & Beloborodov, A. M. 2017, *ARA&A*, **55**, 261
- Kauffmann, G., Heckman, T. M., Tremonti, C., et al. 2003, *MNRAS*, **346**, 1055
- Keimpema, A., Kettenis, M. M., Pogrebenko, S. V., et al. 2015, *ExA*, **39**, 259
- Kennicutt, R. C., Jr. 1998, *ApJ*, **498**, 541
- Kewley, L. J., Dopita, M. A., Sutherland, R. S., Heisler, C. A., & Trevena, J. 2001, *ApJ*, **556**, 121
- Kewley, L. J., Jansen, R. A., & Geller, M. J. 2005, *PASP*, **117**, 227
- Kirsten, F., Marcote, B., Nimmo, K., et al. 2022, *Natur*, **602**, 585
- Kirsten, F., Ould-Boukattine, O. S., Herrmann, W., et al. 2024, *NatAs*, **8**, 337
- Kocz, J., Ravi, V., Catha, M., et al. 2019, *MNRAS*, **489**, 919
- Konijn, D. C., Hewitt, D. M., Hessels, J. W. T., et al. 2024, *MNRAS*, **534**, 3331
- Kothes, R., Sun, X., Gaensler, B., & Reich, W. 2018, *ApJ*, **852**, 54
- Lanman, A. E., Andersen, B. C., Chawla, P., et al. 2022, *ApJ*, **927**, 59
- Lanman, A. E., Andrew, S., Lazda, M., et al. 2024, *AJ*, **168**, 87
- Law, C. J., Sharma, K., Ravi, V., et al. 2024, *ApJ*, **967**, 29
- Leung, C., Andrew, S., Masui, K. W., et al. 2025, *AJ*, **170**, 53
- Leung, C. & CHIME/FRB Collaboration 2025, *ATel*, **17086**, 1
- Li, X. H., & Han, J. L. 2003, *A&A*, **410**, 253
- Lin, H.-H., Scholz, P., Ng, C., et al. 2024, *ApJ*, **975**, 75
- Longair, M. S., & Scheuer, P. A. G. 1970, *MNRAS*, **151**, 45
- Lorimer, D. R., Bailes, M., McLaughlin, M. A., Narkevic, D. J., & Crawford, F. 2007, *Sci*, **318**, 777
- Loudas, N., Li, D., Strauss, M. A., & Leja, J. 2025, arXiv:2502.15566
- Lynden-Bell, D. 1971, *MNRAS*, **155**, 95
- Macquart, J. P., & Ekers, R. 2018, *MNRAS*, **480**, 4211
- Macquart, J. P., Prochaska, J. X., McQuinn, M., et al. 2020, *Natur*, **581**, 391
- Madison, D., Li, W., & Filippenko, A. V. 2008, *CBET*, **1239**, 2
- Mannings, A. G., Fong, W.-f., Simha, S., et al. 2021, *ApJ*, **917**, 75
- Marcote, B., Nimmo, K., Hessels, J. W. T., et al. 2020, *Natur*, **577**, 190
- Marcote, B., Paragi, Z., Hessels, J. W. T., et al. 2017, *ApJL*, **834**, L8
- McGregor, K., & Lorimer, D. R. 2024, *ApJ*, **961**, 10
- McKinven, R., Gaensler, B. M., Michilli, D., et al. 2023, *ApJ*, **950**, 12
- McKinven, R., Michilli, D., Masui, K., et al. 2021, *ApJ*, **920**, 138
- McMullin, J. P., Waters, B., Schiebel, D., Young, W., & Golap, K. 2007, in ASP Conf. Ser. 376, Astronomical Data Analysis Software and Systems XVI, ed. R. A. Shaw, F. Hill, & D. J. Bell (San Francisco, CA: ASP), 127
- Medlock, I., Nagai, D., Singh, P., et al. 2024, *ApJ*, **967**, 32
- Metzger, B. D., Berger, E., & Margalit, B. 2017, *ApJ*, **841**, 14
- Michałowski, M. J., Thöne, C., de Ugarte Postigo, A., et al. 2020, *A&A*, **642**, A84
- Michilli, D., Seymour, A., Hessels, J. W. T., et al. 2018, *Natur*, **553**, 182
- Morgan, J. S., & Ekers, R. 2021, *PASA*, **38**, e013
- Moster, B. P., Naab, T., & White, S. D. M. 2013, *MNRAS*, **428**, 3121
- Nagao, T., Maiolino, R., & Marconi, A. 2006, *A&A*, **459**, 85
- Nakajima, K., Ouchi, M., Xu, Y., et al. 2022, *ApJS*, **262**, 3
- Ng, M. & CHIME/FRB Collaboration 2025, *ATel*, **17081**, 1
- Nimmo, K., Hewitt, D. M., Hessels, J. W. T., et al. 2022, *ApJL*, **927**, L3
- Nimmo, K., Pleunis, Z., Beniamini, P., et al. 2025, *Natur*, **637**, 48
- Niu, C. H., Aggarwal, K., Li, D., et al. 2022, *Natur*, **606**, 873
- Ocker, S. K., Cordes, J. M., Chatterjee, S., et al. 2022, *ApJ*, **931**, 87
- Olausen, S. A., & Kaspi, V. M. 2014, *ApJS*, **212**, 6
- Oppermann, N., Yu, H.-R., & Pen, U.-L. 2018, *MNRAS*, **475**, 5109
- Osterbrock, D. E., & Ferland, G. J. 2006, *Astrophysics of Gaseous Nebulae and Active Galactic Nuclei* (Mill Valley, CA: Univ. Science Books)
- Ould-Boukattine, O. S., Blaauw, R., Buchsteiner, T., et al. 2025, *ATel*, **17124**, 1
- Ould-Boukattine, O. S., Chawla, P., Hessels, J. W. T., et al. 2024, arXiv:2410.17024
- Pandhi, A., Gaensler, B. M., Pleunis, Z., et al. 2025, *ApJ*, **982**, 146
- Pandhi, A., Pleunis, Z., McKinven, R., et al. 2024, *ApJ*, **968**, 50
- Pastorello, A., Pumo, M. L., Navasardyan, H., et al. 2012, *A&A*, **537**, A141
- Pastorello, A., Smartt, S. J., Mattila, S., et al. 2007, *Natur*, **447**, 829
- Pearlman, A. B., CHIME/FRB Collaboration, Gendreau, K. C., et al. 2025a, *ATel*, **17117**, 1
- Pearlman, A. B., Scholz, P., Bethapudi, S., et al. 2025b, *NatAs*, **9**, 111

- Perley, R. A., & Butler, B. J. 2017, [ApJS](#), **230**, 7
- Petrosian, V. 1992, in *Statistical Challenges in Modern Astronomy*, ed. E. D. Feigelson & G. J. Babu (New York: Springer), 173
- Petrov, L. Y., & Kovalev, Y. Y. 2025, [ApJS](#), **276**, 38
- Piro, L., Bruni, G., Troja, E., et al. 2021, [A&A](#), **656**, L15
- Planck Collaboration, Aghanim, N., Akrami, Y., et al. 2020, [A&A](#), **641**, A6
- Pleunis, Z., Good, D. C., Kaspi, V. M., et al. 2021, [ApJ](#), **923**, 1
- Pradeep E. T., S., Sprenger, T., Wucknitz, O., Main, R. A., & Spitler, L. G. 2025, [arXiv:2505.04576](#)
- Prochaska, J. X., Hennawi, J. F., Westfall, K. B., et al. 2020, [JOSS](#), **5**, 2308
- Prochaska, J. X., Macquart, J.-P., McQuinn, M., et al. 2019, [Sci](#), **366**, 231
- Prochaska, J. X., & Zheng, Y. 2019, [MNRAS](#), **485**, 648
- Qian, H., Niu, J. R., Cao, J. H., et al. 2025, [ATel](#), **17126**, 1
- Reynolds, R. J. 1977, [ApJ](#), **216**, 433
- Rhodes, L., van der Horst, A. J., Fender, R., et al. 2020, [MNRAS](#), **496**, 3326
- Ryder, S. D., Bannister, K. W., Bhandari, S., et al. 2023, [Sci](#), **382**, 294
- Sammons, M. W., Deller, A. T., Glowacki, M., et al. 2023, [MNRAS](#), **525**, 5653
- Schlaflly, E. F., & Finkbeiner, D. P. 2011, [ApJ](#), **737**, 103
- Schroeder, G., Rhodes, L., Laskar, T., et al. 2024, [ApJ](#), **970**, 139
- Seymour, A., Michilli, D., & Pleunis, Z., 2019 DM-phase, *Astrophysics Source Code Library*, ascl:1910.004
- Shah, V., Shin, K., Leung, C., et al. 2025, [ApJL](#), **979**, L21
- Sharma, K., Ravi, V., Connor, L., et al. 2024, [Natur](#), **635**, 61
- Shepherd, M. C., Pearson, T. J., & Taylor, G. B. 1994, [BAAS](#), **26**, 987
- Shin, K., Masui, K. W., Bhardwaj, M., et al. 2023, [ApJ](#), **944**, 105
- Simha, S., Eftekhari, T. & CHIME/FRB Collaboration 2025, [ATel](#), **17116**, 1
- Sorce, J. G., Tully, R. B., Courtois, H. M., et al. 2014, [MNRAS](#), **444**, 527
- Speagle, J. S. 2020, [MNRAS](#), **493**, 3132
- Spitler, L. G., Scholz, P., Hessels, J. W. T., et al. 2016, [Natur](#), **531**, 202
- Strolger, L.-G., Dahlen, T., Rodney, S. A., et al. 2015, [ApJ](#), **813**, 93
- Sun, H., Cheng, H. Q., Yi, D. Y., et al. 2025a, [ATel](#), **17100**, 1
- Sun, H., Li, D. Y., Jin, C. C., et al. 2025b, [ATel](#), **17119**, 1
- Taddia, F., Sollerman, J., Razza, A., et al. 2013, [A&A](#), **558**, A143
- Takeuchi, T. T., Yoshikawa, K., & Ishii, T. T. 2000, [ApJS](#), **129**, 1
- Tendulkar, S. P., Bassa, C. G., Cordes, J. M., et al. 2017, [ApJL](#), **834**, L7
- Tendulkar, S. P., Gil de Paz, A., Kirichenko, A. Y., et al. 2021, [ApJL](#), **908**, L12
- Thornton, D., Stappers, B., Bailes, M., et al. 2013, [Sci](#), **341**, 53
- Tian, J., Pastor-Marazuela, I., Rajwade, K. M., et al. 2025, [MNRAS](#), **540**, 1685
- Tohuvavohu, A., Kennea, J. A., Roberts, C. J., et al. 2024, [ApJL](#), **975**, L19
- Trimble, V. 1968, [AJ](#), **73**, 535
- Troja, E., Yang, Y. H., Dichiara, S., Kabir, M. E., & Sun, H. 2025, [ATel](#), **17109**, 1
- Tully, R. B., Courtois, H. M., & Sorce, J. G. 2016, [AJ](#), **152**, 50
- Vanderlinde, K., Liu, A., Gaensler, B., et al. 2019, LRP2020, Canadian Long Range Plan for Astronomy and Astrophysics White Papers W028 (Canadian Astronomical Society), 28
- Villar, V. A., Berger, E., Metzger, B. D., & Guillochon, J. 2017, [ApJ](#), **849**, 70
- Wang, M.-C., Jewell, N. P., & Tsai, W.-Y. 1986, [AnSta](#), **14**, 1597
- Wang, P. F., Han, J. L., Xu, J., et al. 2023, [RAA](#), **23**, 104002
- Weigel, A. K., Schawinski, K., & Bruderer, C. 2016, [MNRAS](#), **459**, 2150
- Whitaker, K. E., van Dokkum, P. G., Brammer, G., & Franx, M. 2012, [ApJL](#), **754**, L29
- Woodroffe, M. 1985, [AnSta](#), **13**, 163
- Yamasaki, S., Goto, T., Ling, C.-T., & Hashimoto, T. 2024, [MNRAS](#), **527**, 11158
- Yang, Y. J., Aryan, A., Chen, T. W., et al. 2025, [ATel](#), **17101**, 1
- Yuan, Z., & Wang, J. 2013, [Ap&SS](#), **345**, 305
- Zevin, M., Nugent, A. E., Adhikari, S., et al. 2022, [ApJL](#), **940**, L18
- Zhang, B. 2014, [ApJL](#), **780**, L21
- Zhang, Y.-K., Li, D., Zhang, B., et al. 2023, [ApJ](#), **955**, 142